On observations of artificial light at night from ground and space

von

Kai Pong Tong

Eine Dissertation zur Erlangung des Grades
Doktor der Naturwissenschaften
am
Institut für Umweltphysik,
Universität Bremen

MMXVI

1. Gutachter	Prof. Dr. Justus Notholt
2. Gutachter	Prof. Dr. Ilja Rückmann
3. Gutachter	Dr. Christopher C.M. Kyba
Betreuer	Dr. Georg Heygster
Datum des Kolloquiums	27. April, 2017

謹 獻 先 祖 父

唐 堆

1924−2012

Abstract

To assess the negative effects of artificial light at night, measurement data are often necessary. These can be acquired from ground or satellite-based measurements.

Satellite-based observations of artificial light have an advantage of global coverage. Since the launch of the Suomi National Polar-orbiting Partnership (s−npp) satellite, the Visible Infrared Imaging Radiometer Suite (viirs) Day-Night Band (dnb) provides a tool for worldwide night time remote sensing for various applications, including artificial light. We used the data in year 2015 from the viirs−dnb sensor to study the angular distribution of artificial light in major cities and metropoles in Europe. Despite encountering some issues, for example low overflight rate with cloud-free sky condition, we are able to investigate the angular distributions of upwelling artificial light emission for 74 regions, almost all of which emit more light near the horizon.

In comparison to satellite-based observations, ground-based measurements can acquire data more frequently. An international campaign studying variations of night sky at 44 worldwide locations was conducted in 2011 and 2012, measuring the night sky using broadband radiometers, the Sky Quality Meters (sqms), and was the first time comparing ground-based night sky measurement in a unified analysis procedure. The presence of artificial light reverses the variation pattern of sky brightness at cloudy nights. Instead of darkening of night sky by blockage of extraterrestrial light sources, clouds backscatter the artificial light emitted from ground, brighting the night sky. Comparison with daytime aerosol measurement data did not yield a consistent relationship between the aerosol content and night sky brightness for the rural site in Cabauw, the Netherlands, but found the brightening of the night sky of Madrid with increasing atmospheric aerosol load.

Long-term monitoring of the night sky enables us to observe the change in skyglow pattern over a long period. Two sqms have been set up in a suburban site and a rural site in Bremen, Germany since December 2011. The night sky of the suburban site is found to be brighter during cloudy nights and becomes darker during the course of the night, which is typical for a light-polluted location. While instrumental issues cannot be ruled out, we found a decrease of sky brightness over a span of about 4.5 years, with a stronger decreasing trend at late hours of the night. For the rural site, the local public and domestic lightings are the dominating light source, contributing to the larger skyglow in the early hours of the night. However, with domestic and public lighting switched off as the night progresses, the variation pattern of the night sky is typical for a location with less light pollution, where the overcast sky is only slightly different in brightness from clear sky. It is suspected that this trend in the change of sky brightness originates from the gradual decrease of output of the public lighting system due to aging, while the progress replacing the public lighting to light-emitting diode (led) devices is slow. An improvement in terms of ecological impacts in the future is therefore not guaranteed.

Contents

List of Figures

List of Tables

1   Introduction

OUR EYES are important organs to interact with the environment, as most of the our activities require visions to accomplish. Since the invention of controlled use of fire, its associated production of light [26] extended the active hours of human beings beyond the daytime. Through the advance of technology and exploration of new sources of energy (e.g. fossil fuels), artificial light became readily available, and takes an important role in modern civilization in everyday life and in cultural aspect. However, excessive use of artificial light at night* has caused problems for astronomers and ecology, as well as affecting health of human beings. Until recent years, these negative impacts did not attract awareness in the field of science and in general public. Despite lacking a consensus for a more precise definition, these collective negative effects by artificial light at night can be called *light pollution*.

* Sometimes abbreviated as ALAN.

1.1   Adverse effects of artificial light at night

AMONG many adverse effects the impact on astronomical observations is the first and the most well-known, shown by evaluations from numerous research groups of observational astronomy. In addition, impacts on human health and ecology, as well as indirect enhancement of other pollution problems, are being actively investigated.

DUE to[†] the wide order of magnitude in variation of brightness between daytime and nighttime, the human being adapted to daylight for millennia and use it as an important *Zeitgeber* (a reference of which biological cycle is regulated upon). The production of melatonin, a hormone which regulates sleep pattern and acts as a strong antioxidant in human body, is triggered when the eyes do not receive a large amount of photons. It has been shown that this triggering mechanism can be suppressed in the presence of artificial light at low level, especially for light at short wavelength, which may lead to disruption of circadian rhythm [64]. Suppression of melatonin excretion by artificial light at night is also thought to indirectly increase the risk of various tumors, for example breast cancer [38, 47, 59]. Inappropriate artificial lighting can also increase the likelihood of development of depression and other psychological problems [54].

THE RESPONSES to different spectral ranges of light among species of animals and plants vary, and there are potential hazards for inappropriate artificial lighting to ecological systems.

Many animal species, for example moths, night-flying birds and sea turtles, are attracted by artificial light sources. In some cases, this can cause disorientations and may eventually cause deaths directly or indirectly [41, 47]. Light pollution also affects reproduction [51] and foraging of animals, which may shift the predator–prey balance.

† This section is about effects on human by *indoor* light, as opposed to *outdoor* light which is the subject of interest in this thesis.
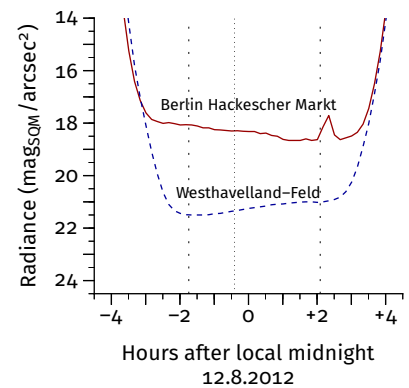
Figure 1.1: Change of sky brightness of a mostly clear, moonlit night in Hackescher Markt, Berlin and at a research field in Westhavelland, State of Brandenburg, Germany with sparse artificial light nearby, when the moon rose at the time indicated by the dotted line. The area enclosed by the dashed line denotes the period without twilight. The sky brightness in Hackescher Markt decreased during the course of the night, even after the moon had risen up from the horizon, whilst the sky in Westhavelland brightens up after the moonrise. The brightness is indicated in a logarithmic radiance unit of $mag_{SQM}/arcsec^2$, which will be discussed in Chapter 2 [33].

Since light pollution is directly related to the increase of number of photons traveling through the atmosphere, this implies that many photochemical reactions involved in air pollution can be influenced during night. For example, nitrate radicals destruction is enhanced in the presence of anthropogenic lights, and ozone concentration increases correspondingly [58, 22]. One of the possible reactions is

$$NO_3 + O_2 \xrightarrow{h\nu} NO_2 + O_3 \qquad (1.1)$$

Some studies exploited the measurement of light pollution by satellite as a method for estimation of energy consumption [37, 40].

1.2   History of artificial light at night and research

The earliest mention of the effect of artificial light appeared around the late 19th century, when *skyglow* was observed over the recently lit streets in Paris*. The term "light pollution" first appeared in the early 1970s, when astronomers in the usa observed the increasing trend of night sky luminance, and sites suitable for astronomical observations became more difficult to find [50]. Before that, studies on effects of artificial light source on animal behaviors took place, some of which can be traced back to mid-1920s [25, 28, 52]. However, it was not before 1990s that more in-depth studies on the subject areas mentioned in the previous sections were conducted.

Quantitative studies of light pollution often involve analyses of remote sensing images obtained by satellites. In late 1990s and 2000s one of the most common choices was the Defense Meteorological Satellite Program (DMSP) operated by the National Oceanic and Atmospheric Administration (NOAA). Since the Operational Linescan System (OLS) on-board the DMSP satellites is capable to observe radiation in the visible light, it is suitable for large-area upwelling artificial light measurements at a wavelength band between 440 nm and 940 nm [14]. However, the gain setting of the OLS is normally variable and not recorded, and is thus not radiometrically calibrated. Calibrated measurement at low fixed gain setting could only be done under permission of NOAA [14]. This problem was overcome with the commissioning of the Suomi National Polar-orbiting Partnership (S-NPP) satellite in 2011. The Visible Infrared Imaging Radiometer Suite (VIIRS) on-board this satellite comprises sensors with known gain settings and on-board radiometric calibration. One of the sensors is the panchromatic Day–Night Band (DNB), which is capable of both daytime and nighttime imaging at a much higher spatial resolution (742 m) and analog-to-digital bit depth (14 bits) than the DMSP (2.5 km and 6 bits, respectively) [8][†]. At the expense of temporal coverage, nighttime satellite images with even higher resolution can also be acquired from spacecraft at lower orbits. The International Space Station (ISS), for example, can be used as a platform for nighttime imaging using commercially available digital cameras, with resolution ranging from 750 m to 1.5 m [60].

Aerial Imagery at a scale of city can also be conducted when better spatial resolution is needed. This has been undertaken in many major cities around the world, for example Berlin [30] and Las Vegas [19]. However, due to high operation cost, temporal coverage is limited.

* Personal communication with Sara B. Pritchard, Cornell University, NY, usa during the the 3rd International Conference on Artificial Light at Night, 2015, Sherbrooke, Canada.

† The details of the viirs–dnb sensor will be discussed in Chapter 3.

ADVANCES in imaging sensors also enables low-cost, high-resolution imagery from the ground at high acquisition frequency in the order of one minute, which helps quantifying and simulating skyglow [35], measuring all-sky brightness [17] and extinction of extraterrestrial light sources [3], as well as spectrum of the skyglow [5].

There are several ground-based large-scale surveys and measurement campaigns dedicated for the quantification of artificial light at night. The largest project of this type is the GLOBE at Night project [34]*. Volunteers compare the night sky observed by naked eye with provided night sky charts for classifying the night sky brightness, or measuring the zenith night sky brightness using low-cost portable optical radiometers, namely the Sky Quality Meters (SQMs) manufactured in Canada by Unihedron†. Another project with similar goal is the *Buiometria Partecipativa* ‡ (BMP, in English Participatory Sky Quality Measurement) of Italy, which invites volunteers from the country for measuring the night sky brightness of different locations using the SQMs since 2008. This approach had also been deployed by the University of Hong Kong for the project *A Survey of Light Pollution in Hong Kong* [55, 57]. Some continuous measurement networks also exist, for example the *Verlust der Nacht* project which operates a network in Berlin§, the *Hong Kong Night Sky Brightness Monitoring Network* (HKNSN)¶, and the expansion of the network for East Asia, *the Globe at Night - Sky Brightness Monitoring Network***.

* http://www.globeatnight.org

† http://www.unihedron.com

‡ http://www.pibinko.org/bmp2

§ http://www.verlustdernacht.de

¶ http://nightsky.physics.hku.hk

** http://globeatnight-network.org

1.3   Outline

CHAPTER 2 makes an overview of theories relevant to observations of artificial light, including the sources of natural and artificial light at night, factors which can influence the propagation of light, specifically those related to night time light sources, and physical quantities related to measurements of the night sky.

Chapter 3 concerns the potential use of satellite measurements as a means of investigating emission of artificial light at night at different angles. The limitations of currently available satellite measurements for quantifying artificial light will also be discussed.

Chapter 4 recaps the findings in an international night sky measurement campaign in summer 2011 and 2012 by Kyba et al. [33], in which I analyzed the measurement data. How aerosols can influence the measured sky brightness will also be briefly investigated using a subset of data in the study.

Chapter 5 describes the details of the long-term measurement carried out in and around Bremen, Germany spanning 4.5 years, to find out changes of sky brightness over the measurements, and postulate the causes of the observed changes.

I conclude in Chapter 6 by summarizing the findings and describing the ecological implications, as well as proposing possible future studies to be carried out locally and globally.

2   *Background*

THE NIGHT SKY naturally varies in a complex way, where many different light sources from space, from upper atmosphere and from ground play important roles in influencing the brightness at different spectral regimes. Other materials on ground and in the air, while not emitting light, can change the propagation of light drastically by reflecting and absorbing photons at different wavelengths. With the introduction of artificial light at night, the pattern of variations becomes even more complex due to the patterns and unpredictability of human behaviors.

In writing this chapter, I extensively used Wikipedia as the starting point for finding literature, as well as a source for quick facts.

Here we will lay down the theoretical basis which will be used to understand both natural and artificial light at night.

2.1   Interactions of photons with matters

MATTERS can interact with photons by emission, scattering and absorption. While the origin of these phenomena must be explained by quantum field theory, it is out of the scope of this thesis, where we are concerned with interactions of photons with matters in the scale of atoms, molecules and particles, present in the atmosphere and the Earth's surface. Also, since we concern mostly visible light, only interactions possible for that regime will be described below.

2.1.1   *Mie scattering and Rayleigh approximation*

IN 1908, Gustav Mie [44] developed a theory of scattering of electromagnetic waves with spherical particles derived from the Maxwell's electromagnetic equations, which resulted in a set of analytical solutions. In atmospheric physics, most scattering and absorbing particles and molecules are in the order of nanometers to hundreds of micrometers. It is useful to define the unitless Mie Parameter, χ, as

$$\chi = \frac{4\pi r}{\lambda} \tag{2.1}$$

where r is the radius of the particle, and λ is the wavelength of the photon. If $\chi \gtrsim 1$, we have to deal with the full solution of the Maxwell's equation. The derivations can be found, apart from the original article of Mie [44], from many textbooks about atmospheric radiations and scattering (see [39, 63] for examples). Here we briefly describe the components of the solution. First we define the extinction efficiency coefficient Q_{ext} as

$$Q_{ext} = Q_{sca} + Q_{abs} \tag{2.2}$$

where Q_{sca} is the scattering efficiency coefficient and Q_{abs} is the absorption efficiency coefficient. Q_{sca} can be expressed as an infinite series of summation as

$$Q_{sca} = \frac{2}{\chi^2} \sum_{n=1}^{\infty} (2n+1)\{|a_n|^2 + |b_n|^2\} \tag{2.3}$$

where $|a_n|$ and $|b_n|$ are complex functions of χ and n and are called *Mie coefficients*.
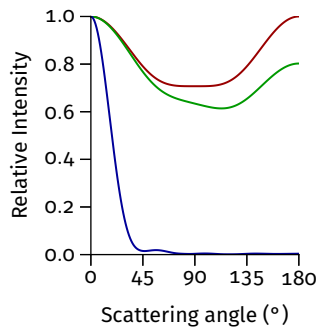
Figure 2.1: Angular distributions of scattered light from a water droplet with Mie parameters χ at $5 \cdot 10^{-5}$ (red), 0.5 (green) and 5 (blue). Code adopted from [10].

If $\chi \ll 1$, then the Rayleigh approximation can be used instead of the full Mie solution. The intensity of the scattered radiation at angle θ can be expressed as

$$I(\theta) = \frac{I_0}{r^2} \alpha^2 \frac{128\pi^5}{3\lambda^4} \frac{P(\theta)}{4\pi} \tag{2.4}$$

where $P(\theta) = 3(1 + \cos^2 \theta)/4$ is the phase function, and α is the polarizability related to the density and the complex refractive index of the medium [39].

2.1.2 Absorption of photons by matters

ATOMS, molecules and particles can also absorb incoming photons. This depends on the structure of the atom, molecule or the particle in concern. For non-ionizing photons and in the case of an atom, a photon is absorbed if the energy of the photon is equal to the difference between two energy states of its electrons. For molecules or particles there are more possibilities of absorbing a photon because they can also oscillate, vibrate and rotate. The treatment of absorbing particles involves the use of Schrödinger Equation, but will not be shown here.

2.2 Propagation of light in a continuous medium

WHEN a photon travels inside a continuous medium, for example inside the atmosphere, it is useful to imagine that the medium is comprised of infinitesimally small cells, and that each cell has integrated optical properties in both extinction and reflection. With this in mind we define the extinction cross section σ_{ext}, which is proportional to the number density of the scattering and absorbing particles in the medium. Then the change in intensity dI for a beam with an initial intensity I_0 traveling inside the medium with a path length of ds, assuming that the medium is homogeneous, is

$$dI = I_0 \sigma_{ext} N ds \tag{2.5}$$

where N is the density of the extincting particles. Integrating this equation yields

$$I = I_0 exp(\sigma_{ext} N) \tag{2.6}$$

This is called Bouguer–Beer–Lambert Law, which describes the attenuation of a photon beam in a medium. With this the optical depth, τ, is defined as

$$\tau = -\sigma_{ext} N \tag{2.7}$$

where the minus sign is to denote that attenuation occurs when τ is positive.

Table 2.1: Composition of the Earth's Atmosphere. Data for dry air only, as water vapor content in the atmosphere can vary. The numbers add up to more than unity due to rounding error and measurement uncertainty [67].

Gas	Percentage by volume
N_2	78.08
O_2	20.95
Ar	0.93
CO_2	0.04
Ne	0.02

2.3 The Earth's Atmosphere

THE EARTH'S ATMOSPHERE, comprising of various molecules and particles, is important in propagation of photons, and is the origin of most of the optical phenomena. Most of the meteorological phenomena happens at the lowest layer of the atmosphere, the troposphere. It is also where the most important effects on propagation of the artificial light occur, including emission, scattering absorption and refraction.

Apart from gases, there are also other substances in liquid, aqueous and solid phase in the atmosphere. Clouds are perhaps the most important

constituent in the atmosphere because their presence can dramatically change the propagation of radiation including the visible light, which is the regime in concern of this thesis. Depending on the size, phase and shape of cloud droplet, the scattering profile of a droplet can vary. Cloud height can further complicate the backscattering of light from terrestrial sources. In addition, atmospheric aerosols also can modify the radiative transfer properties of light.

2.4 Radiometric Basics

RADIANCE is used throughout this thesis. It is defined as the radiant flux per unit area and solid angle, which is usually denoted as L. Radiant flux Φ, in turn, is defined as the radiant energy, or the energy of photons Q, emitted per unit time:

$$\Phi = \frac{dQ}{dt} \tag{2.8}$$

Then we have

$$L = \frac{d\Phi}{d\Omega dA \cos\theta} \tag{2.9}$$

where A is the area and θ is the incidence angle. In International System of Units (SI) it is expressed in W/(sr·m²) [18].

In astronomy, it is often necessary to quantify objects of a wide range of brightnesses. Astronomers express the brightness of an object in logarithmic scale, and define a relative unit, magnitude (mag), by

$$\Delta m = m_1 - m_2 = -2.5 \cdot log_{10}\left(\frac{I_1}{I_2}\right) \tag{2.10}$$

where Δm is the relative brightness in mag, with the brightnesses of two objects I_1 and I_2. A difference of -2.5 mag means an *increase* by a factor of 10 [65]. The reference brightness (0 mag) is defined by that of Vega (α Lyrae).

2.5 Natural night sky

THE NIGHT SKY is naturally not dark. Instead, a lot of natural sources, mostly extraterrestrial, illuminate the sky during the night. Leinert et al. [36] summarized the different sources of diffuse night sky brightness excluding twilight and moonlight. The total night sky brightness, I_{tot}, can be written as

$$I_{tot} = (I_A + I_{ZL} + I_{ISL} + I_{DGL} + I_{EBL})exp(-\tau) + I_{sca} \tag{2.11}$$

where τ is the optical thickness of the atmosphere. The other terms are described as follows:

- Airglow, I_A, occurs in the upper atmosphere. It is caused by excitations of molecules by photolysis and cosmic rays.
- Zodiacal light, I_{ZL}, occurs when interplanetary dust particles scatter the sunlight.
- Integrated star light, I_{ISL}, is starlight not strong enough to be individually distinguishable.
- Diffuse galactic light, I_{DGL}, is the light originating from our galaxy, the *Milky Way*, whereas the Extragalactic background light, I_{EBL}, come from the other galaxies.
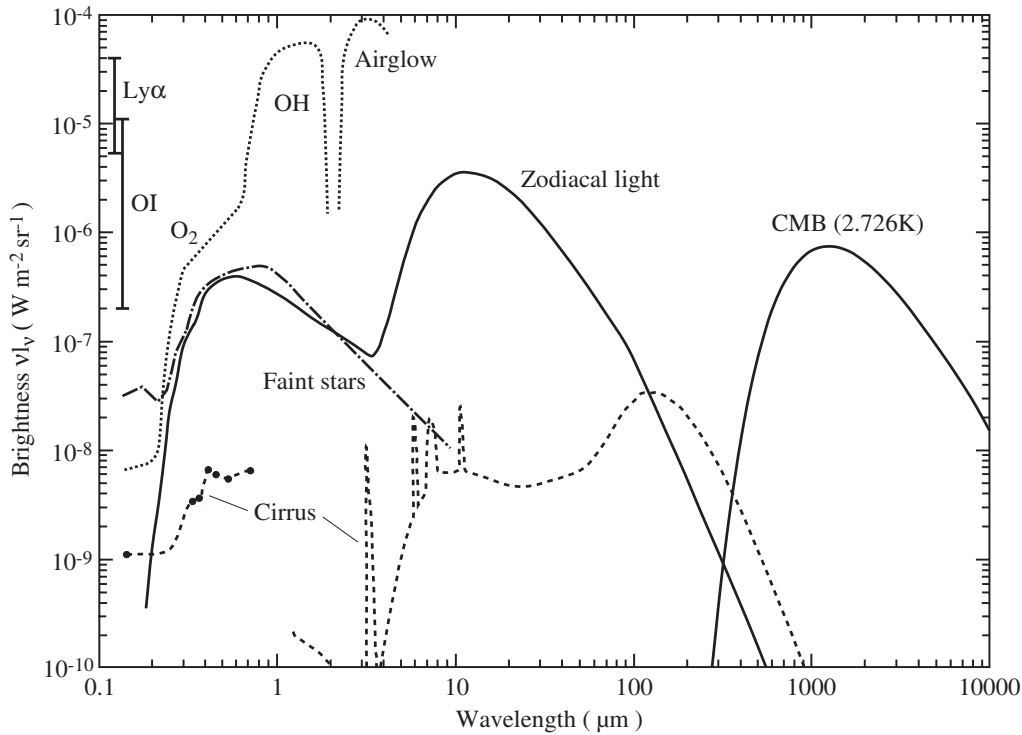
Figure 2.2: Contributions from different natural night time light sources using modeled and experimental data [36]. The wavelength of our concern ranges approximately from 400 nm to 700 nm.

- Scattered light, I_{sca}, can either be caused by the sources stated above, or from artificial light sources.

The total natural sky brightness is not a constant, but instead varies with time. It has been reported [16] that the natural sky brightness can range from 22.2 to 20.0 mag/arcsec².

2.6   Artificial light at night

LIGHTING TECHNOLOGY and urban lighting plan shape the skyglow pattern, for example the emission spectrum and angular distribution. Also important are the topography and the layout of cities. Although the contribution of the skyglow from indoor commercial and domestic light sources are not negligible, we will focus on major outdoor light sources below.

Most of the public lighting systems in developed countries, apart from several major cities, are electrically powered. The advance in lighting technology increased the energy efficiency of the public lighting system, as well as changing the emission spectra, since they work with different underlying principles. Earlier electric lighting systems, as well as florescent lighting, involve the excitation of mercury vapor. They typically have emission peaks at 435.8 nm and 546 nm [46]. For high output applications, sodium vapors are used, with a major emission lines at 589.0 nm and 589.6 nm. High-pressure sodium (HPS) lamps, which are often used in modern fixtures, have more emission lines. With the advent of recent developments in semicondutor-based lighting, the deployment of light-emitting diode (LED) lightings are surging, partly due to their potentially high energy efficiency. LEDs's emission spectrum can be engineered by controlling the doping of
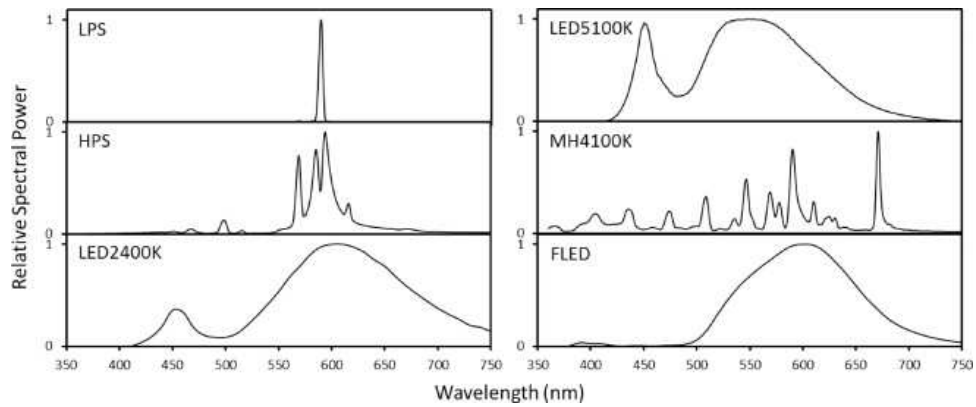
Figure 2.3: Emission spectra for various light sources. Shown here are low-pressure sodium (LPS), high-pressure sodium (HPS), LED lights with a correlated color temperatures (CCT) of 2,400 K and 5,100 K, metal halide lamp with a CCT of 4,100 K (MH4100K), and a filtered white LED with sharp cutoff at short wavelength (FLED) [42].

the cathode, and "white" light (broadband emission) can be achieved by adding phosphor in front of the cathode of a blue LED, which is widely used in outdoor applications for public lighting. However, most of the white LED emit a large amount of blue light which can increase the skyglow [42].

Some existing light pollution models have made predictions of propagation of artificial light under various lighting and meteorological conditions, most of which use the technique of radiative transfer modeling. Some models, like the ILLUMINA [6], predicted that the effect on skyglow far away from the center of emission depends on not only the aerosol content, but also the angular distribution of emission of the light sources and obstacle height. In addition, higher blue content can worsen the skyglow, especially at short distance. The presence of clouds are also studied by some models. Kocifaj and Solano Lamphar [29], for example, found in an numerical experiment that cloud height and type can influence the increase of skyglow under cloudy sky, and that the increase in sky brightness has a sharp increase near the city boundary.

3   *Measurement of angular distribution for artificial light in Europe by satellite-based remote sensing*

To accurately understand and model skyglow patterns, it is important to know how various factors affect the emission and propagation of artificial light at night. One of these significant but less studied variables is the angular distribution of upwelling artificial light, which is only considered by some studies in sensor calibration [7], but not in annual or monthly wide-area survey. Also important is the change of emitted artificial light during the progress of the night.

As discussed in Chapter 1, the successful launch and deployment of the satellite Suomi NPP and its on-board instrument VIIRS enables acquisition of radiometrically calibrated nighttime images for wide-area light pollution studies. This chapter discusses the use of VIIRS–DNB data in attempt for quantifying the angular distribution of upwelling artificial light at night in Europe, as well as verifying if the effects of aerosols on propagation of artificial light at night can be observed.

3.1   The spacecraft Suomi NPP

THE SPACECRAFT SUOMI NPP was launched on 28th October, 2011 from the Vandenberg Air Force Base, CA, USA atop a Delta II 7920–10C launch vehicle (flight number 357). As of 2nd May, 2016 it is on a sun-synchronous orbit with an inclination of 98.7°, an apogee of 835 km and a perigee of 819 km. The satellite has a local equator-crossing time of approximately 1:30 and orbits the Earth once every 101.8 minutes. Apart from VIIRS, it also carries the Advanced Technology Microwave Sounder (ATMS), a microwave radiometer, the Cross-track Infrared Sounder (CrIS), a Michelson interferometer, the Ozone Mapping and Profiler Suite (OMPS), an imaging spectrometer for ozone measurement, and the Clouds and the Earth's Radiant Energy System (CERES), a radiometer measuring global radiative energy balance. It weighted 2,270 kg at launch and, as of this writing, has exceeded its expected service life of five years. The Suomi NPP serves as a prototype of the Joint Polar Satellite System (JPSS), with the first operational satellite, the JPSS–1, scheduled for launch in 2017.

THE VIIRS INSTRUMENT is a 22-channel radiometer imaging the Earth's surface for visible to thermal infrared (TIR) radiation (Table 3.1). All detectors for the VIIRS instrument share a single optical assembly comprising the Rotating Telescope Aseembly (RTA) and the Half Angle Mirror rotating half the rate of the RTA, with a solar diffuser and a blackbody calibrator as radiometric calibration sources. Of the 22 channels, 16 are used for radiometry with a nadir resolution of approximately 750 m, and five for imaging with a nadir resolution of approximately 375 m.

Table 3.1: Available channels of the VIIRS instrument [69].

Channel	Wavelength (nm)
DNB	500–900
M1	402–422
M2	436–454
M3	478–498
M4	545–565
M5	662–682
M6	739–754
M7	846–885
M8	1,230–1,250
M9	1,371–1,386
M10	1,580–1,640
M11	2,225–2,275
M12	3,660–3,840
M13	3,973–4,128
M14	8,400–8,700
M15	10,263–11,263
M16	11,538–12,488
I1	400–680
I2	846–885
I3	1,580–1,640
I4	3,550–3,930
I5	10,500–12,400

The DNB channel, comprising a cooled charged couple device (CCD) sensor, is a broadband radiometer with a full width-half maximum wavelength from 500 to 900 nm. By using a variable subpixel sampling scheme, the DNB maintains an almost constant spatial resolution of 742 m across scan. With three different gain stages, DNB has a dynamic range in integrated spectral radiance of 3 nW/(sr · cm²) to at least 20 mW/(sr · cm²) [1], and can measure during both day and night.
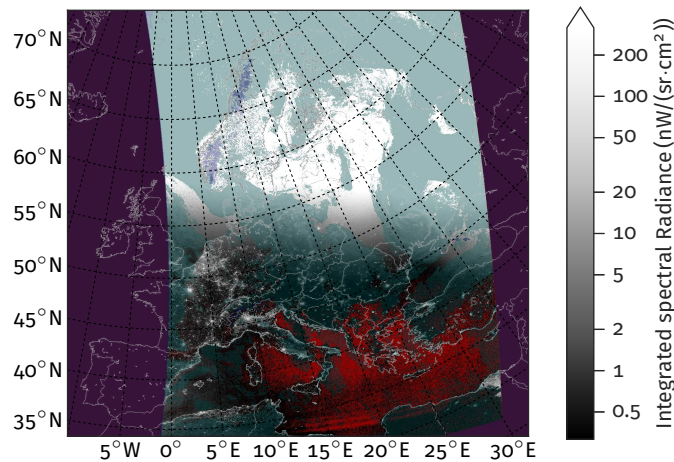
Figure 3.1: Single overflight image for 28 June, 2015. VIIRS cloud mask is shown by cyan hue, and snow mask by blue hue. Red indicates lower than zero integrated spectral radiance. The red bands toward the bottom of the image is possibly caused by alternate over and undercorrection of stray light.

Several issues were identified with the measurements using the VIIRS–DNB post-launch. The sensor performs its radiometric calibration using the solar diffuser when the spacecraft is sunlit, and zero integrated spectral radiance point calibration is performed with the night view when the spacecraft is over the unhabilitated area of the southern Pacific Ocean, to avoid possible artificial light sources. However, due to the presence of airglow, the radiometric calibration may sometimes result in positive linear offset of integrated spectral radiance value* appearing as negative integrated spectral radiance values at unlit areas. The DNB sensor's spectral sensitivity is known to be dependent on gain stages, mainly due to the use of neutral density (ND) filter for the low-gain stage. However, since the data used for this analysis came only from those taken after astronomical twilight, data taken in low-gain stage were not involved. Also to be considered is stray light contamination, which arises from direct sunlight entering the optical path of the system when the sun is below the horizon on ground level, but above the horizon at the spacecraft's altitude. Since 21st August, 2013 NOAA and Northrope Grumman apply a stray light correction algorithm, improving the signal to noise ratio for data point when solar zenith angle is larger than 105°. However, the variance of the stray light-corrected data are different from stray light-free data, hinted by strips of possible over and undercorrections shown in Figure 3.1. In this analysis, however, we only

* Personal communication with Kimberly Baugh, National Center for Environmental Information (NCEI), NOAA, during discussions in LPTMM 2015.

consider cases where upwelling artificial light at night is significant. The effect of overcorrection is thus not considered here.

3.2 Data synergy

The summary of the flow for the synergy of the viirs–dnb-derived angular distribution map is shown here:

VIIRS–DNB sensor data record (SDR)
VIIRS cloud mask intermediate product
Geolocation metadata

↓ *Gridding*

Gridded integrated spectral radiance maps
Gridded cloud and snow masks

↓ *Cloud and snow filtering*

Cloud & snow-masked integrated spectral radiance maps

Pixel-by-pixel averaging over satellite zenith angles ↓   ↓ *Binning by satellite zenith angle*

All satellite zenith angle mean integrated spectral radiance map   13 satellite zenith angle-binned grid cell-wise mean integrated spectral radiance maps

Thresholding by integrated spectral radiance Morphological closing ↓   ↓ *In-bin averaging*

Map of regions of interests   Binned mean radiance maps

↓   ↓ *Filtering grid cells not present in all bins Averging over selected grid cells*

Data of angular distribution for upwelling light

Figure 3.2: Flow chart for producing the viirs–dnb angular distribution map.

The details of the procedure is described below.

3.2.1 *Integrated spectral radiance data*

The viirs–dnb sensor data record (sdr) used in this analysis was generated either by the Space Science Engineering Center (ssec) of the University of Wisconsin–Madison (no longer available as of this writing) or noaa's National Center for Environmental Information (ncei), both of which calculated from raw data record (rdr) containing not only scientific data, but also diagnostic and telemetry data. The data are available in Hierarchical Data Format hdf5, which are internally GZip-compressed to save storage space. The dnb data are accompanied by geolocation metadata consisting of coordinates of the pixels, elevation, spacecraft position, motion and attitude, and solar and lunar parameters. Geolocations are terrain-corrected after 22nd May, 2014. In addition, several quality flags are included in the sdr files, however none of them is used in this analysis. As a result of the huge file size of the data (more than 100 GiB/day*), external download tools, namely the WebAPI written by ssec of the University of Wisconsin–Madison and noaa's Comprehensive Large Array-Data Stewardship System (class)†, were used to find out granules of integrated spectral radiance and gelocation data relevant to this analysis.

* GiB means gibibyte (binary gigabyte), which is 2^{30} bytes.

† http://www.class.ncdc.noaa.gov

Each of the DNB granule comprises of 4,064 pixels across track and 768 pixels along track. The SDR data have to be gridded in order to carry out analyses for fixed locations such as those in the scale of village, district, town or city. When gridding the data, the convenience of performing future analyses was also considered — the projection has to be of equal area per grid so that quantities like integrated spectral radiance can be easily compared, and it has to cover most of the Earth's surface so that minimal sets of projection schemes are needed when extending the analyses. The Equal-Area Scalable Earth Grid (EASE-Grid) 2.0 [11] was chosen due to the reasons above. In addition, the datum used by EASE-Grid 2.0 is World Geodetic System (WGS) 84, which is also used by most of the common projection systems. To match the resolution of the DNB sensor and prevent from interpolation artifacts, nearest-neighbor interpolation was performed with a grid length of approximately 750 m. The gridded area and its projection is shown in Figure 3.3.
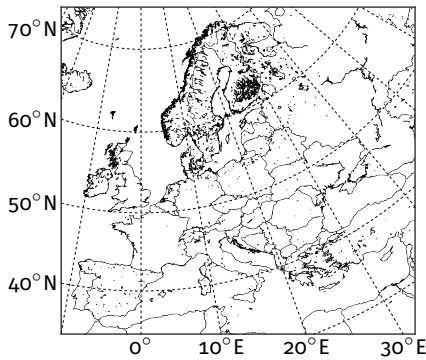
Figure 3.3: Area and projection of the study.

3.2.2   Cloud data

During nighttime, the thermal emission bands M12 (3.61–3.79 µm), M14 (8.4–8.7 µm), M15 (10.26–11.26 µm) and M16 (11.54–12.49 µm), are used by the VIIRS cloud mask intermediate product (IP) upstream of the cloud optical thickness and effective particle size retrievals environmental data record (EDR) [2]. The algorithm uses thermal emission channels and differences of these channels to determine the presence of clouds, considering also the surface type and classifies individual pixels into four different categories: confidently cloudy, probably cloudy, probably clear and confidently clear.

Like most of the VIIRS data products, the cloud mask IP also has several quality flags which record the quality of cloud mask, presence of sun glint and cirrus clouds, and some general cloud properties.

3.2.3   Composites of upwelling light angular distribution

At different overflights a given surface element of the Earth is observed under different zenith and azimuth angles. This allows to analyze the angular distribution of upwelling artificial light at night, but it is necessary to first generate composite images binned into a sufficiently small range of satellite zenith angle, so that the angular distributions of different regions can be easily compared.

Several criteria have to be met in order for a DNB pixel to be included in the composite images. First, because this analysis is sensitive to weak light sources, twilight and moonlight must be absent for the position at the Earth's surface. When an area's sun elevation angle is above –18° or when the moon is above the horizon, the observation for the area is not used. Secondly, the area must be absent of clouds as reported by the cloud mask. This was done by selecting only pixels flagged as "confidently clear". However, due to the scattering of particulate matter the VIIRS cloud mask may show false positives in some highly populated areas caused by emissions and smog. A method based only upon a fixed threshold in integrated spectral radiance was used to tackle this problem: if the integrated spectral radiance of a pixel is higher than 40 nW/(sr·cm²), then the pixel was also selected when it was classified as "probably clear". This is possible because

brightly lit areas are also likely to be more populated with more severe air pollution.

The data were initially binned by satellite zenith angle at an increment of 1°. This produced stripy composite images not usable for this analysis but was necessary because they were needed to manually determine suitable bin sizes. After visual check the data were rebinned at ±8° at nadir, ±6° at 14° and ±5° beyond, resulting in 13 symmetrically arranged bins. As a result of the larger than 90° inclination angle of the Suomi NPP satellite, the azimuth angle goes from the east to the west as the night progresses for the same surface element on the Earth's surface.

3.2.4 *Identifying and characterizing regions of interest*

A threshold based on minimum mean integrated spectral radiance, using all available clear sky data in 2015 independent of satellite zenith angle, was used to select bright regions, with the threshold set at 5 nW/(sr·cm²), which is about 170% of the design detection limit of the instrument [1]*. These selected grid cells were connected by performing a morphological closing operation with a radius of 1 grid cell, in order to reduce the chance that a city was identified as multiple regions of interest, which can arise by varying land uses and extent of urbanization. More than 45,000 regions of interest with an area of at least 1 grid cell (approximately 0.57 km²) were identified by this method. Cities which are selected as regions of interests are named using the data from the website GeoNames†. The center of each region of interest is calculated by the mean of the grid coordinates separately for each axis, then a search of the nearest region of interest for each entry in the GeoNames database with populations larger than 100,000 is performed, with higher priority for cities with larger populations. After that, a manual check for some regions of interests are carried out to correct or assign the names of the nearest major cities.

* Later studies show lower than expected detection limit, being able to detect airglow and auroras. See for example [45].

† http://www.geonames.org

After selecting a subset of grid cells which has at least one cloudless overflight in all the available satellite zenith angle bins, the mean of the mean integrated spectral radiance among these grid cells were calculated for each satellite zenith angle bin, together with the standard deviation of the integrated spectral radiance of the grid cells. In order to quantify the general characteristics of the upwelling light emission for each of the major regions of interests, a quadratic fit of upwelling integrated spectral radiance with respect to the satellite zenith angle is performed in the form of

$$L_{fit}(\theta) = a\theta^2 + b\theta + L_{fit,nadir} \tag{3.1}$$

where a, b are the quadratic and linear coefficients, and $L_{fit,nadir}$ is the fitted nadir upwelling integrated spectral radiance in the unit of nW/(sr·cm²). Here a positive θ denotes a satellite zenith angle to the east. A positive a coefficient indicates higher integrated spectral radiance at higher satellite zenith angle (or slant angle), and vice versa. The b coefficient shows asymmetry of emission at different directions. As the Suomi NPP satellite travels to the west relative to a specific position on the Earth with the progression of time, a non-zero b coefficient may also imply that the emission for a region of interest changes in the course of the night, as shown in ground-based night sky measurements (Chapter 4).

To save computation time and to minimize the effect of instrumental uncertainty and geolocation uncertainty, calculations are only done for 74 regions of interests larger than 800 grid cells (approximately 450 km²).

3.2.5   Comparison with ground-based aerosol measurement data

To verify if the presence of aerosols can affect the pattern of upwelling light, daytime aerosol optical depth (AOD) data from the Aerosol Robotic Network (AERONET) [24] are downloaded. The mean AOD as well as the Angström exponent, which quantifies the dependence of AOD with respect to wavelength, in the years 2014 and 2015 for individual measurements are calculated for the nearest AERONET station within 10 km of each region of interest. The AOD values used for the reading routine is for the green regime of the spectrum of human vision. This regime of wavelength is used to correspond to the peak response of the Sky Quality Meter (SQM)*. If one of the channels 531 nm, 532 nm, 551 nm or 555 nm is present for the sunphotometer used in a station, the AOD values will be used directly to represent the atmospheric aerosol content. Otherwise, the AOD value is interpolated to the value for 540 nm, the wavelength of peak response of the SQM, using the measured Angström exponent

$$\tau_{540\,nm} = \tau_{\lambda_0} \cdot \left(\frac{540\,nm}{\lambda_0}\right)^{\alpha_{\lambda_0}} \tag{3.2}$$

Here $\tau_{540\,nm}$ is the AOD at 540 nm, τ_{λ_0} is the AOD at the wavelength λ_0 and α_{λ_0} is the Angström exponent at λ_0. If there are more than one channels available between 340 and 1,640 nm, the calculated AODs from the two channels nearest to 540 nm are averaged to yield the reading. To compensate for the extinction of upwelling artificial light by the aerosol content of the atmosphere, the mean integrated spectral radiance for different satellite zenith angle bins are then recalculated by

$$L_{cor}(\theta) = L(\theta) \cdot exp(\frac{\tau_{540\,nm}}{\cos\theta}) \tag{3.3}$$

where $L_{cor}(\theta)$ is the aerosol-corrected mean integrated spectral radiance, and $\frac{1}{\cos\theta}$ is the *air mass factor*, which accounts for the lengthening of the optical path in the atmosphere at a slant angle. The quadratic fit parameters are also recalculated for each region of interest with

$$L_{cor,fit}(\theta) = a_{cor}\theta^2 + b_{cor}\theta + L_{cor,fit,nadir} \tag{3.4}$$

where the subscript $_{cor}$ denotes the respective parameters after compensation for atmospheric aerosols.

3.3   Results and discussion

COMPOSITE MAPS of the plot area at nadir and at 65° ±5° from the west are shown in Figures 3.4 and 3.5 respectively. Some stable but highly variable natural light sources, such as aurora, can be seen at higher latitudes. Also noticeable is that the VIIRS snow mask does not only filter out data taken when snow cover is present, but also the areas where surface albedo is high, for example most of the area in northern Africa, except for the populated areas like the Nile Delta, which typically have lower surface albedo. In Figure

* The measurements made by SQMS will be discussed in Chapters 4 and 5.
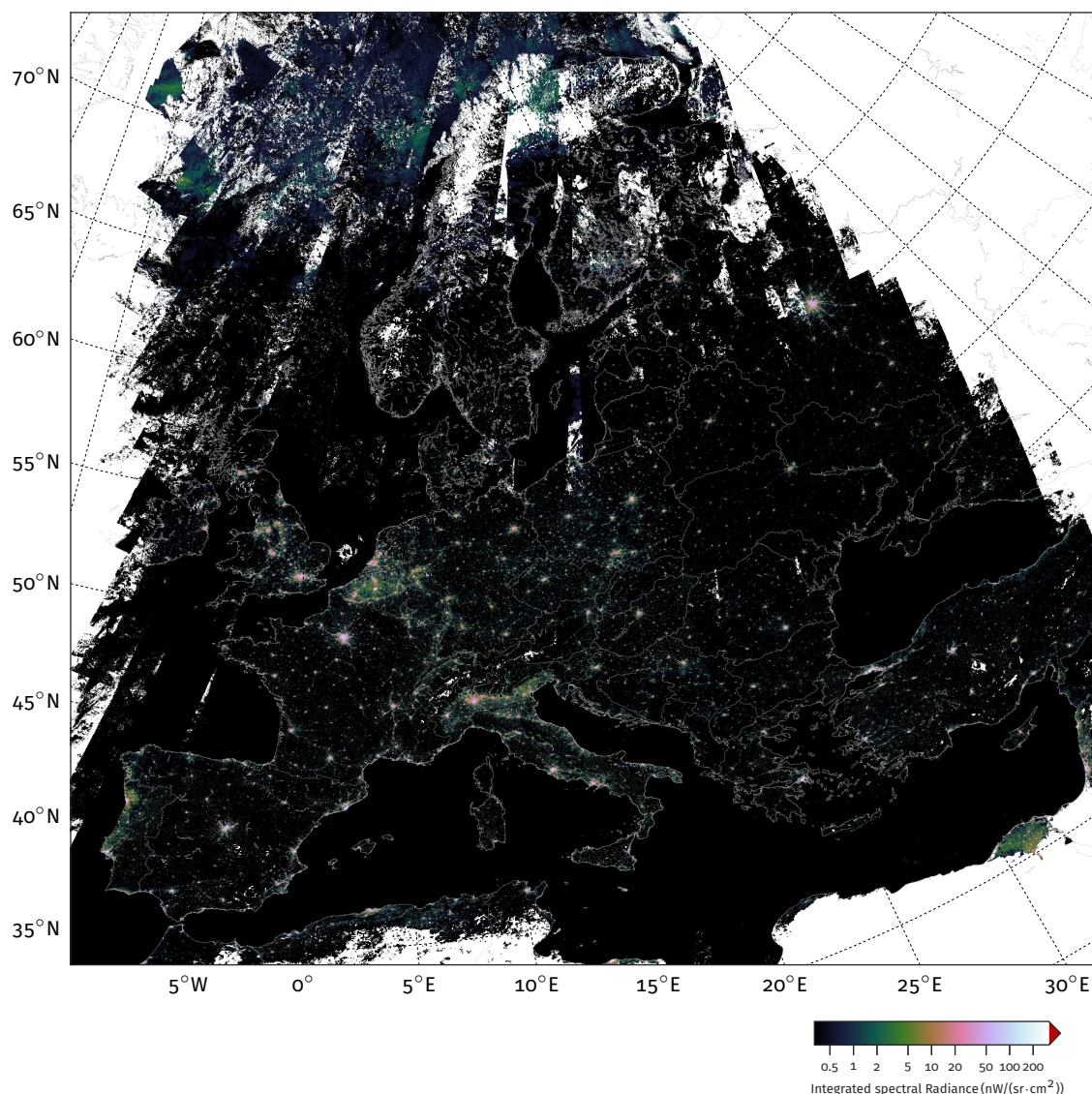
Figure 3.4: Composite VIIRS–DNB image of integrated spectral radiance for year 2015 at nadir±8°. Data are screened by VIIRS cloud and snow mask, and no data are included when ground level sun elevation angle is above −18° or when the moon is above the horizon.

3.5, data is missing at the west end of the plot area because the SDR data at the western scan edge were not downloaded. An attempt to download data from NOAA's CLASS server for the area by including data in later hours yielded only few additional overflights, and the range in time was thus not further extended. Similar extended area of missing data is seen also at the east end of the plot area for the overflights near the eastern scan edge.

The angular distributions of 74 regions of interests larger than 450 km² and smaller than 11,250 km², which include some of the largest cities and metropolitan areas in Europe, are shown in Figure 3.6, and the corresponding mean numbers of overflights for individual bins shown in 3.7. Since the area in consideration also includes some part of the Middle East and North Africa, some major cities in these areas are also present in this analysis. Explicitly excluded area is the Northern Italy in the southern part of the Alps
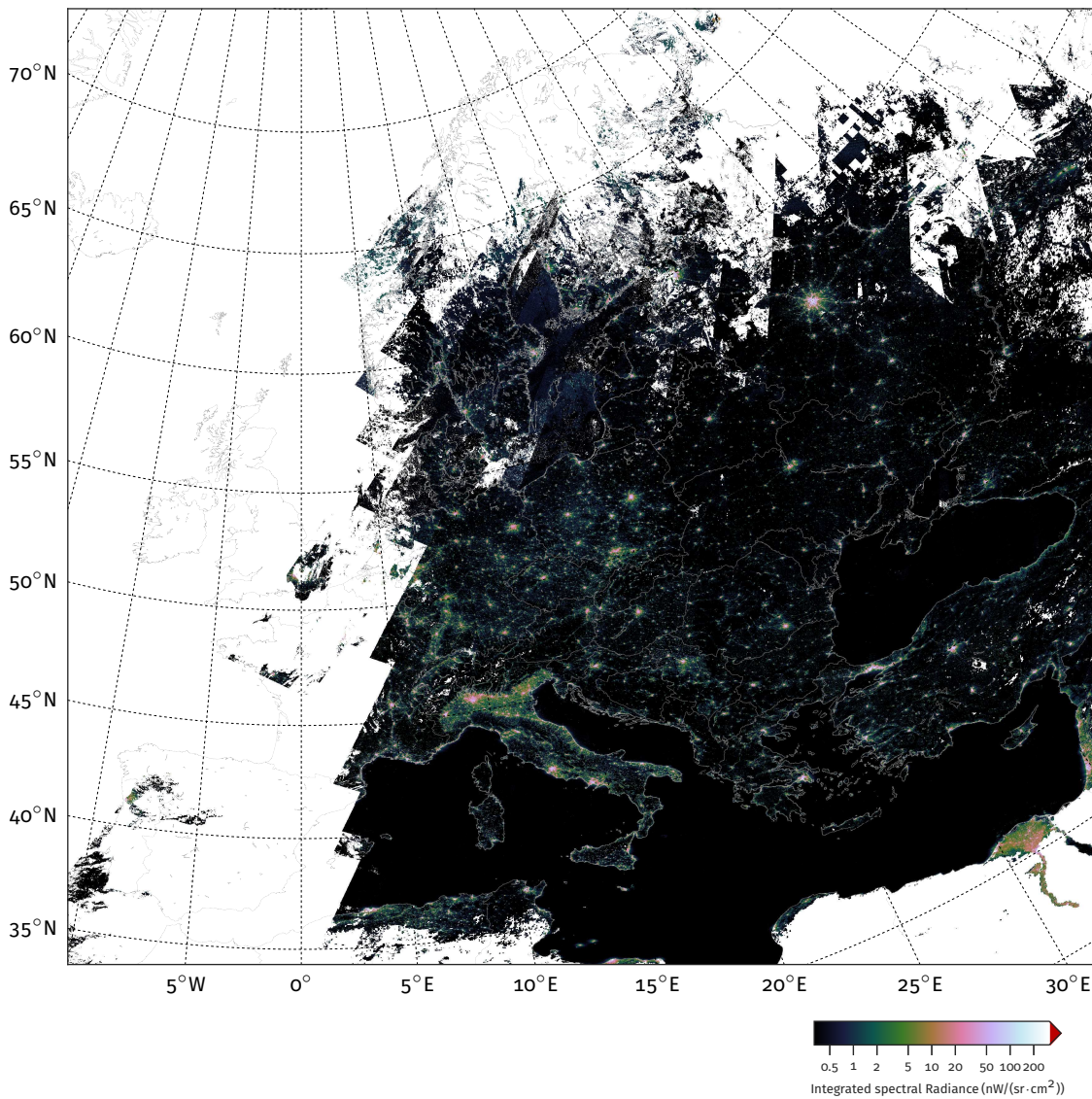
Figure 3.5: Composite VIIRS−DNB image of integrated spectral radiance for year 2015 at 65° ±5° from nadir with the same data reduction criteria as 3.4. Area on the west end shows more missing data due to problem in downloading and data being taken in later hours of the night.

* The cities and towns may be separated when some image processing routines specialized in distinguishing individual objects in an image are used (e.g. `scikit-image` package in `Python`), however higher level image processing routines are not yet done in this study, and should be considered in follow-on investigations.

because the area of interest connects multiple cities and towns as a single region*. Noticeable from the figure is that the uncertainty of the calculated mean integrated spectral radiance are in most cases larger than the variation in the mean integrated spectral radiance at different satellite zenith angles. This may be caused by the inherent instrumental uncertainty of VIIRS−DNB, which is 100% at lower detection limit and 30% at the upper detection limit of the low-gain stage, determined by preflight test [1].

The mean numbers of overflights are found to be between 1 and 19 (found in Bari, Italy. See Figure 3.7). With a survey period of one year, this amounts to roughly 1.6 overflights per month. Some of the bins in the regions of interests only had one overflight. There are several causes with the low number of overflights, apart from failure of downloading more data as mentioned above. First, the routines and WebAPI used for downloading
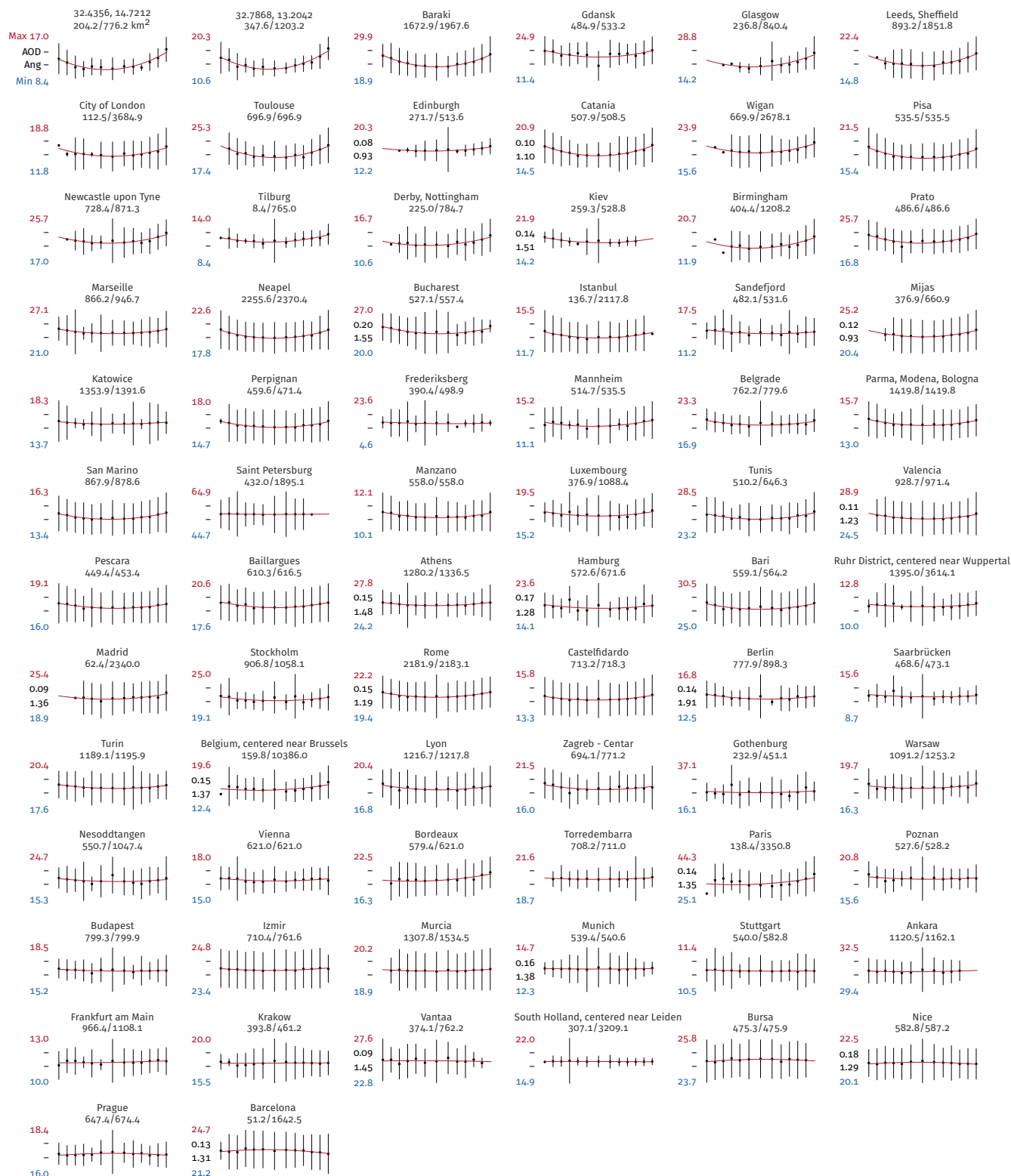
Figure 3.6: VIIRS–DNB retrieved angular distribution of upwelling artificial light at night for regions of interests larger than 450 km² and smaller than 11,250 km², arranged from left to right, top to bottom with descending b/L_{fit}. All plots are in relative scale in the y-axis, with the numbers in red and blue showing the maximum and minimum mean integrated spectral radiance among the bins in each respective region of interest in the unit of nW/(sr·cm²). The red lines show the quadratic fits. The bins are centered symmetrically at nadir, 14°, 25°, 35°, 45°, 55° and 65° arranged from the west on the left towards the east. Average values of AODs and Angström exponents in years 2014 and 2015 are also shown when AERONET measurements are available. Area common to all available bins and total area for each region of interest are indicated.

Figure 3.7: Mean numbers of overflights of viirs–dnb for regions of interests shown in Figure 3.6 with the same arrangement. The maximum (red) and minimum (blue) mean number of overflights among the bins of each region of interest are also shown.
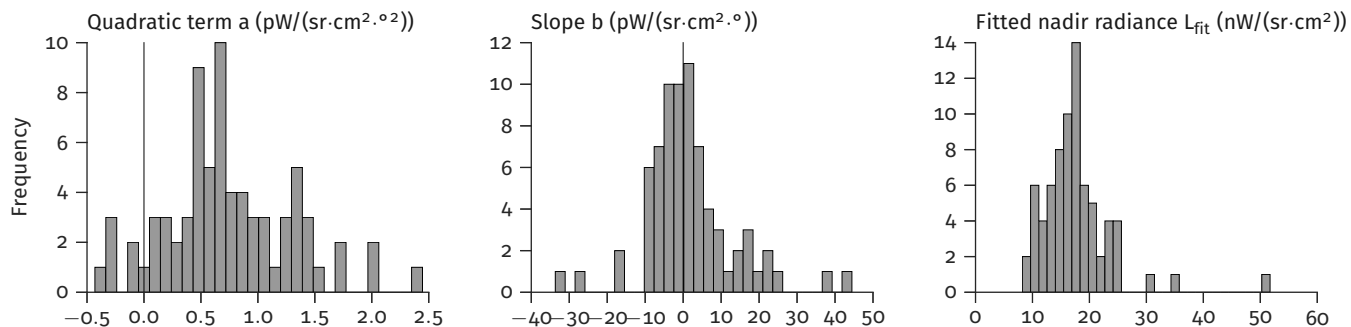
Figure 3.8: Histograms for quadratic fit parameters. Vertical lines on the histograms for quadratic term and slope indicate zero points.

the appropriate granules of night time VIIRS–DNB data may ignore some of the overflights near the scan edge of the area of analysis, which explains why some of the regions of interests at the west side of the area of analysis show significantly lower numbers of overflights when the satellite is in the west direction (e.g. London, Madrid, Paris). Second, the number of *usable* overflights depends greatly on the sky condition. An example is Hamburg (Figure 3.7, row 7, column 4), which is situated in the northern Germany with relatively few periods of clear sky, had only in average one to eight overflights among the available grid cells across all zenith angle bins in year 2015, or less than 0.5 overflights per month. Third, that this analysis uses only scenes without moonlight or twilight reduces the amount of available data further. The small amount of available data affects the robustness of the results obtained in the analysis.

By contrast, in the calculation of the 2nd World Atlas of Artificial Light [20], Falchi et al. used all available overflights not cloud-contaminated or with moonlight or twilight, except those at high satellite zenith angle (to avoid data points with lower signal-to-noise ratio), without binning according to time of overflight or satellite zenith angle. This increased the statistical base of the dataset, but it leaves the user with the uncertainty about the variability of the radiance with these parameters.

The histograms of the fit parameters for the regions of interest, which are represented by the red curves in Figure 3.6 are shown in Figure 3.8. Of the 74 analyzed regions of interest, all but six have positive quadratic terms. Since there are insufficient AERONET measurements with large aerosol content variability, and that night time aerosol measurements by light detection and ranging (LiDAR) devices are sparse, we cannot conclusively find out the causes. However, there are several probable causes. Firstly, the signal-to-noise ratio of the VIIRS–DNB sensor is known to be lower at higher satellite zenith angle [8]. This is a compromise made to the accuracy of the measurements in order to achieve an approximately constant spatial resolution across the scan line, with pixels near to the scan edge using less subpixels. Also, as measurements made at higher zenith angles involve larger air mass and longer path length, the probability of photons scattered or refracted into the line of sight from artificial light sources also increases. Further, the height of the buildings inside the city, as well as the angular emission profile of the light fixtures can play a role in the upwelling angular
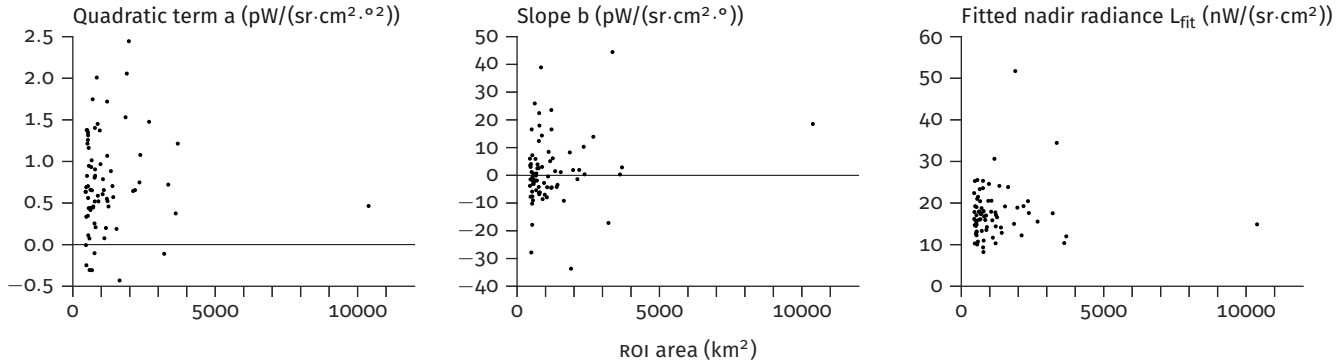
Figure 3.9: Quadratic fit parameters plotted against area of regions of interests. Vertical lines on the plots for quadratic term and slope indicate zero points.

distribution. The buildings act as obstacles, and the height of the buildings can influence how much light is blocked near the horizon, while a fixture with higher upward light output ratio can directly emit more light above the horizon [4]. Moreover, other natural, stable yet highly variable light sources such as airglow may play a role, especially at high latitude where terrestrial magnetic field is stronger. In addition, considering that the local equator crossing time of the Suomi NPP satellite happens after the midnight, when most of the indoor lightings are switched off, it can be expected that emission near the horizon is higher than that acquired by VIIRS–DNB.

For the fitted slope b, 37 of the 74 investigated regions of interests have positive values, which may mean that for the regions of interests we investigate, we find the equal numbers of sites which brighten or darken during the period of night with overflights of Suomi NPP. The average slope among these sites is $+1.5\,\mathrm{pW/(sr \cdot cm^2 \cdot {}^{o2})}$, meaning a slight decrease in integrated spectral radiance over the course of the night. Although this finding is not statistically significant, it is in agreement with ground-based observations as found in Chapter 4. It should be noted that, however, the maximum possible number of overflights for all shown regions of interests is two per night. With an orbiting period of 101.8 minutes this means that only a small period of time after the midnight can be observed.

Figure 3.9 shows the fit parameters, against the area of the region of interest. All three parameters are found to not depend on the area of the region of interest. The amount of upwelling light at different angles depends on various factors, such as the type of lighting used in the city, height of the obstacles, terrain of the city, which are found by Aubé [4] in a numerical experiment, although the simulation he used was done for an hypothetical observer on the ground level.

Figure 3.10a and 3.10b shows the fitted quadratic term a against AERONET mean AOD and Angström exponent for 17 regions of interests with AERONET AOD data respectively. Both parameters show weakly negative correlation coefficients, possibly due to low variability of the AOD and Angström exponent.

With the mean integrated spectral radiance data multiplied by the mean AOD and air mass factor (Figure 3.11), all 17 regions of interests, three of which with negative quadratic term a for the fitted curve before the multiplication, now have positive a_{cor} (Figure 3.12), meaning the emission for

(a)   (b)
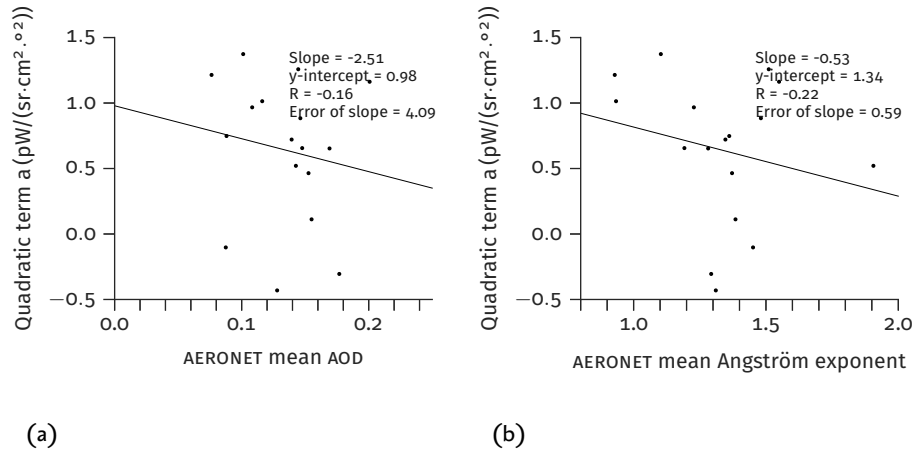
Figure 3.10: Quadratic term a of fits against AERONET (a) mean AODs and (b) mean Angström exponents for measurements in years 2014 and 2015. All AERONET stations are within 10 km from the center of the regions of interests.
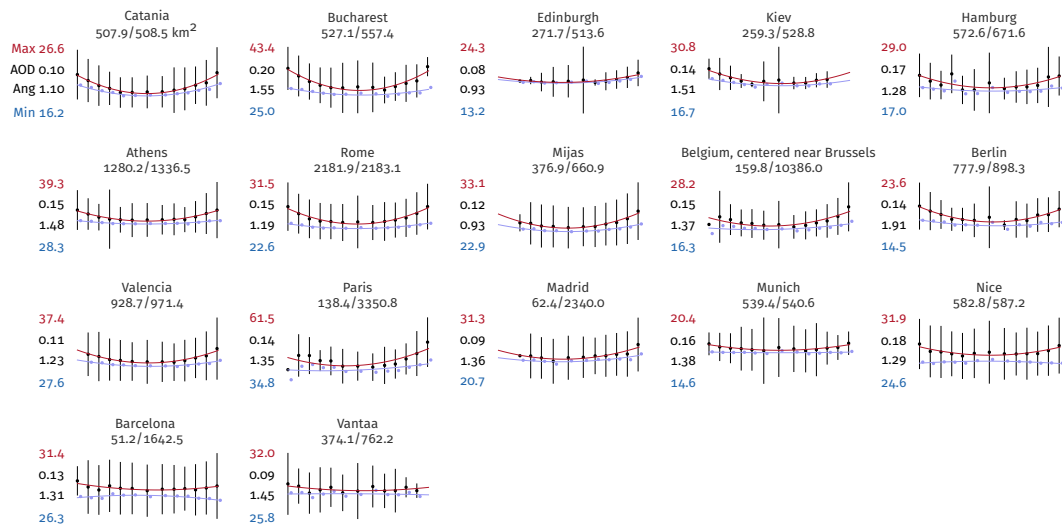
Figure 3.11: VIIRS–DNB retrieved angular distribution of upwelling artificial light at night for regions of interests larger than 450 km² and smaller than 11,250 km² compensated with mean AERONET AOD and air mass factor, arranged from left to right, top to bottom with descending $b_{cor}/L_{cor,fit}$. The plotting scheme is the same as Figure 3.6. Only regions of interests with AERONET AOD data in 2014 and 2015 are shown here. Data before the compensation is shown in pale blue.

all these regions are higher near the horizon. Although the low correlation between the AOD values and the quadratic term prevents us to draw concrete conclusions, it appears that the other regions of interests in Figure 3.6 which show negative a values may actually also emit more at higher zenith angles.

Although the high uncertainty of the measurements renders the observation of angular distributions statistically insignificant, there is an evidence from aerial survey that the observation is plausible. In July 2011, Kyba et al. [31] conducted an aerial survey in order to find out the angular distribution of the upwelling artificial light at night. For both of the east and west directions, they found that the emission of Berlin, Germany (the VIIRS–DNB-retrieved data of which can be found in Figure 3.13) peaks at high zenith angle, at approximately 70°. In the VIIRS–DNB composite data, although the peak is at the nadir, the gradual increase of integrated spectral radiance can also be seen towards the scan edge.
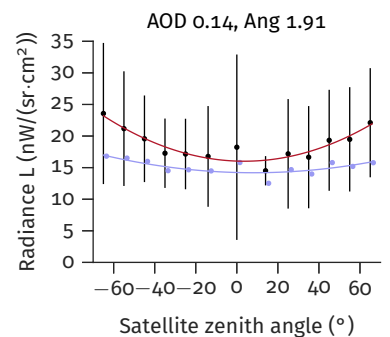
Figure 3.13: VIIRS–DNB retrived angular distribution of upwelling artificial light at night for Berlin as shown in Figure 3.11, Row 2, Column 5.
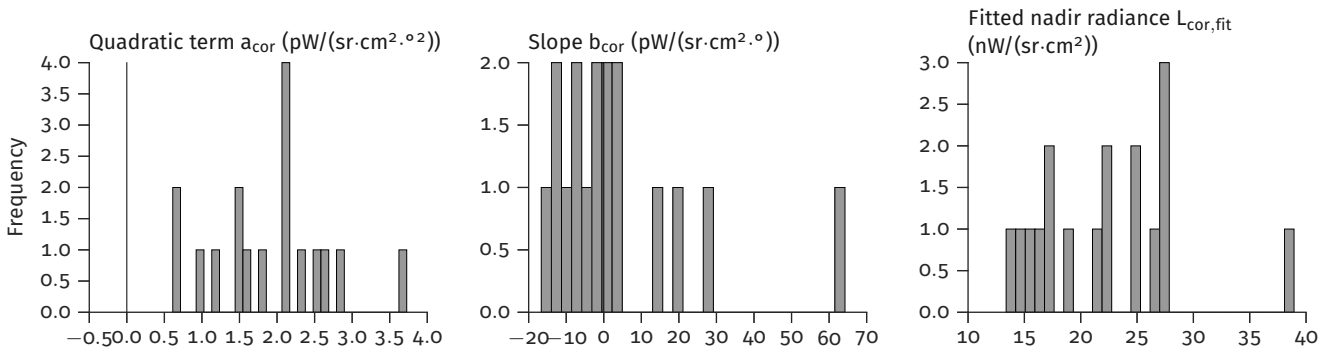
Figure 3.12: Histograms for quadratic fit parameters with integrated spectral radiance compensated by mean AERONET AOD and air mass factor. The plotting scheme is the same as Figure 3.8. Only 17 regions of interests with AERONET AOD data in 2014 and 2015 are selected.

3.4   Summary

THE public availability of calibrated night time brightness data offered by the VIIRS–DNB opens up the opportunity of quantifying artificial light at night for wide areas around the world. Compared to its predecessor, the Optical Linescan System (OLS), it has a higher analog-to-digital bit depth, and records also the gain settings with radiometric calibration. There are some technical limitations to the instruments. As it is a broadband sensor it cannot detect the spectra of the upwelling light, and is insensitive to light below 500 nm in wavelength. Also, the uncertainty in measurements is high. While these may hamper some in-detail studies for night time phenomena requiring accurate measurements, we are able to use the data taken in 2015 to find that most of the major cities in Europe emit more artificial light at higher zenith angle. Similar analyses can be carried out for the data taken by Suomi NPP's successor, the JPSS satellites. Since emitted light traveling at high zenith angle can travel far away from the source in the atmosphere, this means that not only the nocturnal animals inside or near the cities can be affected by the artificial light at night, but also those far away from the cities. With the continuing advance of sensors, it is possible that future satellite remote sensing missions dedicated to night time measurements can make improvements in accuracy of measurements and provide spectrally more resolved measurements for wide-area light pollution studies.

4 Variation of night sky measured by ground-based instruments

SATELLITE OBSERVATIONS, while being able to cover a wide area, have low repeat cycle relative to ground-based measurements: that of the VIIRS instrument, for example, is approximately 16 days, while ground-based instruments like a typical stationary scanning spectrometer or an automated Sky Quality Meter (SQM) can measure ranging from once every several hours to once every second. Also, as demonstrated in the last chapter, the uncertainty associated with satellite-based measurements, like those with VIIRS–DNB, is higher than ground-based measurements. Due to these factors, various effects from geographic and demographic factors, for example lighting technology, social behaviorial difference, topographical and geographical characteristics, climatologial and meteorological influences, cannot be determined solely by means of satellite-based remote sensing. In addition, the use of ground-based artificial light measurements can serve as ground truth for verification purpose.

Since the introduction of low-cost instruments like the SQMs and commercially available digital cameras, it becomes easier to do long-term and wide area ground-based survey.

In 2011 and 2012, night sky radiance data were collected from 50 sites around the world, and analyzed in a unified procedure. The results are published in [33]. This chapter describes the details about the procedure of the analysis, as well as the follow-on work on finding out the relationship between aerosol content and sky brightness.

4.1 Instrument for zenith night sky measurement — the Sky Quality Meter

THE SQM is a low-cost, broadband and wide field-of-view radiometer designed to mainly measure zenith sky radiance during the night. It consists of an infrared filter (Hoya CM-500-IR) used to decrease the sensitivity in the infrared regime, an integrated light-to-frequency converter consisting a silicon photodiode and a current-to-frequency converter (Texas Advanced Optoelectronic Solutions TSL-237), a temperature sensor for thermal noise correction and a network controller. A conical plastic focusing lens, which is used in all devices involved in this thesis, narrows the field-of-view of the sensor to 20° full-width-half-maximum (FWHM). Newer devices from year 2015 and on use hemispherical glass lenses to avoid UV aging problem found on some older devices [61]*. The instrument has a wavelength of peak sensitivity at approximately 540 nm, with a spectral response designed to be similar but not identical to photopic human vision [15] and the definition of visual magnitude [27]. Therefore we denote the unit of the SQM measurements as $\mathrm{mag_{SQM}/arcsec^2}$.

Figure 4.1: Isometric view of SQM-LE [62].

* This will be further discussed in Chapter 5.
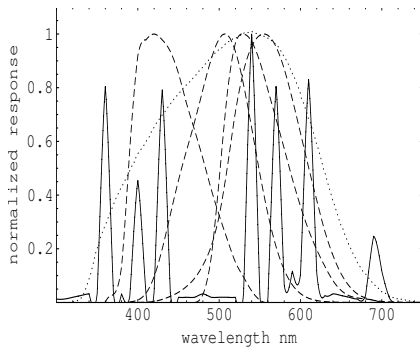
Figure 4.2: Spectral response of SQM (dotted) in comparison with (dashed, from left to right) Johnson B-band, International Commission on Illumination (CIE) scotopic band, Johnson V-band and CIE photopic band. The solid line shows the spectrum of a HPS lamp[12].

Figures 4.2 [12] and 4.3 [13] show the spectral and angular response curves for the SQM respectively. The uncertainty, according to the specifications of the manufacturer, is 0.10 $\text{mag}_{SQM}/\text{arcsec}^2$ (approximately 10%).
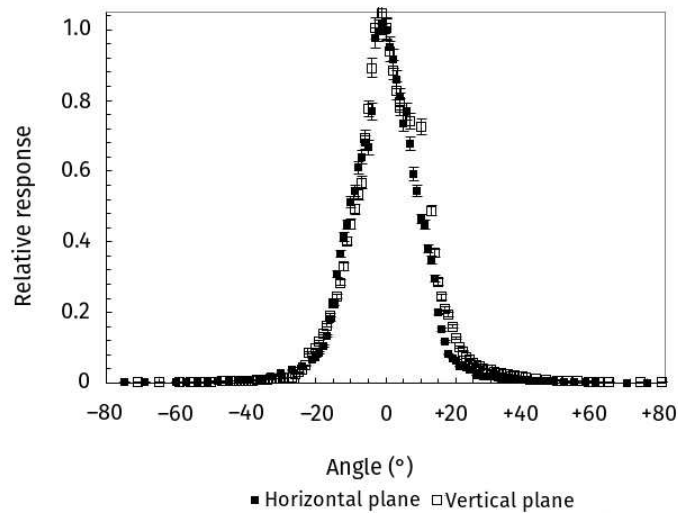
Figure 4.3: Angular response of SQM-L [13].

Figure 4.4: SQM-LE with manufacturer-supplied housing, mounted, pointing towards the zenith for night sky measurement [62].

The SQM is not waterproof by design because it was originally used to make handheld, manually triggered measurements under clear sky to quantify "sky quality", the darkness of a location for astronomical observations, before the connected models of SQMs were introduced. Early adopters of the connected SQM models used custom waterproof housings to contain both the instrument and network equipment, an example of which can be seen in [56], to accommodate adverse weather. A compact waterproof housing (Figure 4.4) was later introduced by the manufacturer, which is designed to also house small networking equipment, for example a power-over-Ethernet (PoE) adaptor to ease the setup for the network connection and power supply, or a dry battery adaptor for data-logging model. A marine grade glass window is attached by silicone sealant on the lid of the housing, 43 mm in diameter, providing the SQM a view of the zenith. Measurement made by the manufacturer shows an attenuation value of 0.11 $\text{mag}_{SQM}/\text{arcsec}^2$.

Table 4.1: Location information for the 50 sites participated in the international SQM measurement campaign. Two SQMs were involved for each of the sites Deerlick, USA and Steglitz, Berlin, Germany. The sites are ordered by increasing observed sky brightness [33].

N	Site name	Description	Loc
1	Tucson KP	Kitt Peak, Tucson, AZ	US
2	Schiermnk	Schiermonnikoog	NL
3	Veinto Rg	Veinto Ridge, Silver City, NM	US
4	Tucson Hpk	Mount Hopkins, Tucson AZ	US
5	Winer	Winer Observatory, Sonoita, AZ	US
6	Alice Sp	Alice Springs	AU
7	IP Feld	Westhavelland, Brandenburg	DE
8	Tucson Lm	Mount Lemmon, Tucson, AZ	US
9	Parey	Parey, Brandenburg	DE
10	Tenerife	STELLA Robotic Observatory, Izana, Tenerife	ES
11	Springendal	Springendal, Hezingen	NL
12	Rad Kwk	Radio Kootwijk	NL
13	Seebergen	Seebergen, Lilienthal	DE
14	Tucson W	Tucson West, AZ	US
15	Calgary RAO	Rothney Astrophysical Observatory Calgary	CA
16	Vitto Veneto	Central Vittorio Veneto	IT
17	Arkemheen	Arkemheen	NL
18	CESAR	Cabauw Experimental Site for Atmospheric Research (CESAR), Cabauw	NL
19	Potsdam Bb	Babelsberg, Potsdam	DE
20	Arnhem	Arnhem	NL
21	Vestby	Vestby	NO
22	Lendinara	Lendinara	IT
23	Berlin Sd	Schulzendorf, Berlin	DE
24	Tucson N	Tucson North, AZ	US
25	Grimsby	Grimsby, ON	CA
26	Met Monte	MeteoMontebello	IT
27	Castigli	Castiglioncello	IT
28	Nove	Nove	IT
29	Bremen H-L	Horn–Lehe, Bremen	DE
30	Morehead	Morehead, KY	US
31	Hamilton	Hamilton, ON	CA
32	Berlin St LE	Steglitz, Berlin (SQM-LE)	DE
33	Berlin St LU	Steglitz, Berlin (SQM-LU)	DE
34	Adelaide	Adelaide	AU
35	Tucson E	Tucson East, AZ	US
36	Tucson C	Tucson Center, AZ	US
37	Utrecht	Utrecht	NL
38	Vienna IFA	Institute of Astronomy, University of Vienna	AT
39	Schipluiden	Schipluiden	NL
40	Plymouth Dv	Plymouth University, Plymouth	UK
41	Tucson S	Tucson South, AZ	US
42	Berlin HM	Hackescher Markt, Berlin	DE
43	Madrid UCM	Universidad Complutense de Madrid, Madrid	ES
44	Edmonton	Edmonton, AB	CA
45	Vlaardingen	Vlaardingen	NL
46	Yonago[¶]	Yonago	JP
47	Mexico[¶]	San Luis Potosì	MX
48	Plymouth Rm[†]	Ramehead, Torpoint, Cornwall	UK
49	Plymouth Mk[†]	Looe, Cornwall	UK
50	FOA Schöpfl[‡]	Leopold-Figl-Observatorium für Astrophysik, Mt. Mitterschöpfl	AT
51	Deerlick 1[§]	Deerlick Astronomical Village, Crawfordville, GA (Station 1)	US
52	Deerlick 2[§]	Deerlick Astronomical Village, Crawfordville, GA (Station 2)	US

[¶] Window attenuation unknown

[†] Thresholding problem

[‡] Instrument failure under dark skies.

[§] Instrument failure

Table 4.2: Detailed information for participating sites in the international SQM campaign, including their geolocations (latitude, longitude, elevation), as well as information about the instrument uptime. Columns "2011" and "2012" show the percentage of time during the study period for which the instruments were online. The column "Up (%)" shows the ratio between the time online and the time which the instrument was expected to acquire data [33].

N	Site name	Loc	Class	Lat (°N)	Lon (°E)	Elev (m)	2011	2012	Up (%)
1	Tucson KP	US	rural	31.96	−111.60	2065	N/A	74.4	99.3
2	Schiermnk	NL	rural	53.48	6.20	7	37.3	93.0	67.7
3	Veinto Rg	US	rural	32.77	−108.33	1936	81.7	N/A	81.7
4	Tucson Hpk	US	rural	31.68	−110.88	2335	N/A	68.0	88.7
5	Winer	US	rural	31.67	−110.60	1516	27.7	15.5	30.8
6	Alice Sp	AU	rural	−23.50	133.84	718	99.8	N/A	99.8
7	IP Feld	DE	rural	52.70	12.46	27	N/A	91.0	91.0
8	Tucson Lm	US	rural	32.44	−110.79	2781	N/A	66.4	89.1
9	Parey	DE	rural	52.68	12.25	36	N/A	82.4	82.4
10	Tenerife	ES	rural	28.30	−16.51	2380	N/A	91.4	91.4
11	Springendal	NL	rural	52.43	6.88	74	80.8	90.3	90.0
12	Rad Kwk	NL	rural	52.11	5.49	71	67.0	27.3	49.7
13	Seebergen	DE	rural	53.14	8.99	11	N/A	86.3	91.8
14	Tucson W	US	suburban	32.24	−111.08	856	N/A	65.6	85.5
15	Calgary RAO	CA	rural	50.87	−114.29	1269	N/A	19.0	19.0
16	Vitto Veneto	IT	suburban	46.01	12.31	500	6.2	34.0	20.1
17	Arkemheen	NL	rural	52.25	5.43	4	75.6	89.8	87.2
18	CESAR	NL	rural	51.97	4.93	3	94.5	73.2	88.7
19	Potsdam Bb	DE	suburban	52.40	13.10	66	97.9	100.0	99.0
20	Arnhem	NL	suburban	51.94	5.87	14	93.4	88.9	96.5
21	Vestby	NO	suburban	59.60	10.76	84	96.7	99.8	99.1
22	Lendinara	IT	suburban	45.08	11.56	9	78.4	7.3	42.8
23	Berlin Sd	DE	suburban	52.36	13.59	50	N/A	90.1	90.1
24	Tucson N	US	suburban	32.32	−111.89	863	N/A	22.2	28.7
25	Grimsby	CA	suburban	43.18	−79.52	173	98.7	99.0	98.9
26	Met Monte	IT	suburban	45.47	11.35	212	72.7	96.1	84.4
27	Castigli	IT	suburban	43.41	10.42	15	85.1	N/A	85.1
28	Nove	IT	suburban	45.71	11.68	87	56.0	94.1	75.1
29	Bremen H-L	DE	suburban	53.10	8.85	22	N/A	79.9	79.9
30	Morehead	US	rural	38.19	−83.44	243	11.0	55.0	11.0
31	Hamilton	CA	suburban	43.27	−79.96	99	98.6	N/A	98.6
32	Berlin St LE	DE	urban	52.46	13.31	91	81.7	1.4	42.7
33	Berlin St LU	DE	urban	52.46	13.31	77	91.4	98.7	98.1
34	Adelaide	AU	rural	−34.62	138.46	25	N/A	40.6	40.6
35	Tucson E	US	suburban	32.23	−110.80	796	N/A	23.4	29.9
36	Tucson C	US	urban	32.23	−110.95	745	N/A	66.8	84.6
37	Utrecht	NL	urban	52.08	5.11	6	69.0	89.3	54.6
38	Vienna IFA	AT	suburban	48.23	16.33	240	N/A	95.6	95.6
39	Schipluiden	NL	rural	51.99	4.28	1	88.3	87.4	92.9
40	Plymouth Dv	UK	urban	50.37	−4.14	36	N/A	98.1	98.1
41	Tucson S	US	suburban	32.11	−110.96	784	N/A	27.0	42.8
42	Berlin HM	DE	urban	52.52	13.40	46	N/A	90.0	90.0
43	Madrid UCM	ES	urban	40.45	−3.73	650	N/A	46.5	46.5
44	Edmonton	CA	urban	53.53	−113.53	695	N/A	53.6	53.6
45	Vlaardingen	NL	suburban	51.91	4.32	4	61.7	88.5	79.6
46	Yonago¶	JP	suburban	35.46	133.29	24	49.8	N/A	49.8
47	Mexico¶	MX	urban	22.14	−101.03	1950	93.6	N/A	93.6
48	Plymouth Rm†	UK	rural	50.32	−4.22	97	N/A	68.3	68.3
49	Plymouth Mk†	UK	rural	50.37	−4.41	134	N/A	50.8	50.8
50	FOA Schöpfl‡	AT	rural	48.08	15.92	880	N/A	100.0	100.0
51	Deerlick 1§	US	pristine	33.56	−82.76	192	39.6	N/A	39.6
52	Deerlick 2§	US	pristine	33.56	−82.76	192	59.5	90.9	75.2

¶ Window attenuation unknown
† Thresholding problem
‡ Instrument failure under dark skies.
§ Instrument failure

4.2 Data acquisition

In total, 54 sqms were involved in the campaign (Tables 4.1 and 4.2), acquiring data from 50 geolocations. Most of the sites were situated in Europe and the usa, with the exception of four sites (two in Australia, one each in Japan and Mexico). Out of the data of the 50 sites, six were found to be either taken by defective devices, or not have information about the attenuation of the housing's window. Thus, the number of sites used in the main analysis was reduced to 44.

To minimize the influence of the change of surface albedo to the night sky radiance only data from the summer months, between May and September in the years 2011 and 2012, of the Northern Hemisphere were used. This does not apply to the two Australian sites situated in Alice Springs and Adelaide, where the whole dataset provided by the site owner were used. Unlike many of the sites in the Northern Hemisphere, snowfall is absent for the two Australian sites, decreasing the seasonal change of night sky radiance. Depending on the type of devices and the network and storage resources, acquisition rates of radiance data varied from once every 15 minutes to once every second.

4.3 Data processing and analysis

The datasets came from different providers. By the time the study was commenced, no standardized data format for recording was present*. Therefore, in order to facilitate unified procedure to analyze the datasets, the data files from the measurements of individual sites were first converted to a unified format using `Python` scripts written for individual dataset, sometimes having to consider glitches and change in data format during the data acquisition period.

For each of the dataset, the average frequency of measurement was first determined. If more than one measurements per minute were made, then the minute-by-minute median of the individual measurements were first taken. Doing this also mitigates the problem of artifact in analog-to-digital conversion, which is caused by electromagnetic interference and inverse proportionality between error in readings and integration time[†]. Later examination of the data, however, showed that the uncertainty caused by quantization artifact is much lower than that of the variation of sky brightness, and was therefore not considered in the uncertainty analysis. Using the `PyEphem` library written in `Python`, the solar and lunar elevation angle for each measurement were calculated, with measurements taken without astronomical twilight (solar elevation angle below $-18°$) and moonlight to avoid the influence of dominating natural light sources. The calculations were made assuming there is no atmosphere, neglecting the effect of atmospheric refraction.

To investigate the effect of presence of clouds to the sky brightness, weather data issued by weather stations were used. This was done by downloading the World Meteorological Organization (wmo) synop[‡] data from the online weather database ogimet[§]. synop reports are issued every six hours minimum per requirements stipulated by the wmo, and some of the weather stations issue as frequently as once per hour. The selection of a

* As an effort to facilitate exchange of night sky measurement data, the International Dark-Sky Association (ida) adopted a text-based standardized data format in September, 2012. The details of the format can be found at `http://darksky.org/wp-content/uploads/bsk-pdf-manager/47_SKYGLOW_DEFINITIONS.PDF`.

[†] The details about quantization artifact and its treatment can be found in [62].

[‡] fm-12 synop (Synoptic surface observation) is an alphanumeric code standardized by the wmo for reporting surface weather from a manned or automatic fixed land station. Detailed information of the code can be found on [68].

[§] `http://www.ogimet.com`

weather station was based on the shortest great circle distance from the sqm measurement site, as well as the data availability. The distances between the weather stations and the sqm sites range from 3 to 112 km. Since some weather stations are far away from the sqm sites, deviation of cloud coverage should be expected.

With the cloud coverage data at hand, the sqm measurement data were assigned with the fraction of cloud coverage in oktas (one eighth of the sky). Since the spatial distribution of clouds can be highly variable in time and horizontally when the sky is neither completely clear nor completely overcast, only measurements taken when cloud cover was either 0 or 8 oktas were used. To avoid outliers from influencing the retrieved values, which can be caused by non-geophysical or coincidental events, for example blockage of the optical path by external objects or lightning, the median was used to represent the clear and overcast sky instead of the mean value. The median sky radiance was calculated for 24:00 (midnight) local time for both clear and overcast cases, and for 22:00 and 2:00 local time for clear night cases, in order to compare the change of sky radiance over different periods of the night. The time window for each of the three periods was ±15 minutes, to minimize the deviation of cloud coverage longer before or after observations.

Approximately half of the sites do not have associated weather data for the midnight. For those stations this analysis could not be carried out. However, Kyba et al. [32] found in Berlin that the difference between the sky brightnesses of clear nights to cloudy nights is proportional to how light-polluted a site is, and that in a urban setting, the night sky becomes brighter when the sky is covered by clouds. It is therefore suggested that the variation of sky brightness can be a proxy of the light pollution of a site in addition to the clear night sky brightness. To infer the difference between clear and cloudy sky brightnesses, the 5th and 95th percentile in sky radiance were compared for each site. The 5th percentile radiance occurs during clear nights in urban areas and likely during overcast nights for pristine areas, as there is very little emitted from ground level backscattered by the clouds, and the clouds block the passage of extraterrestrial and ionospheric light sources.

To compare with the prediction of existing night sky models, the median cloud-free sky radiance for each site was compared with the values from the First World Atlas of Artificial Night Sky Brightness [14]. The 28th percentile of the sqm-retrieved night sky radiance, which was found to be the closest match of the average percentile of the median cloud-free sky radiance, was also calculated for each site and compared to the World Atlas data as well, in order to carry out a similar analysis for sites without nearby weather stations.

As a way to exploit the full use of dataset, measured sky radiance for all sites was plotted against hours relative to local midnight as density plots, calculated using Gaussian kernel estimation provided in the `SciPy` package for visual inspection. These plots can be useful for checking the evolution of sky brightness for a site qualitatively, as well as comparing and contrasting patterns of skyglows in different types of sites.

The sqm is designed to measure a relatively homogeneous field. As seen

from Figure 4.3, the sqm's angular response depends on both the zenith and azimuth angle, and under a strong light source the accuracy of reading from an sqm is sensitive to the alignment of the setup, as well as the optical alignment of the lens and the photodiode inside the sensor [62]. As a first approximation, however, a moonlit, overcast sky is more homogeneous than a clear moonlit sky, and can be used to infer the change in sky brightness due to the presence of the moon. Therefore, to observe the influence of the moonlight to the sky brightness, overcast sky radiance within 15 minutes from local midnight was used to generate density plots against the lunar elevation angle for sites with synop data. Median sky radiance were also calculated in each case. To be included in this analysis, there must be at least 40 observations under overcast sky, and at least one of them must be taken under moonlit sky. It should be noted that the restriction in local time means that the moon illumination ratio has a roughly constant relationship with the moon elevation angle, and therefore the results should be treated only qualitatively.

4.4   Comparison with ground-based aerosol data

No aerosol measurement during night were available for the sqm stations, and only could be indirectly inferred by the spread of the sky brightness during the clear nights. As a result no quantitative analysis on aerosol influence was done. To find out if a relationship between the aerosol content in the atmosphere and the sky radiance measured by the sqm, aerosol optical depth (aod) measurement data made by sunphotometers from the aeronet (see also Chapter 3) were used to compare with the variation of radiance.

For the aerosol measurement data in aeronet, the last measurements of aod before the sunset and the first measurements after the sunrise were first averaged, and then linearly interpolated hour by hour. The aod values used were found using Equation 3.2 to match the sqm's wavelength of peak sensitivity. The change in artificial light at night emission with the time of night was also considered, by binning the sky radiance data with an interval of 30 minutes. Also, to make the analysis more robust, instead of using weather data from the synop stations, which could be more than 20 km away from the sqm sites, the standard deviation of the measurement was taken into account in addition, since a completely clear sky with little variation in atmospheric aerosol content is expected to not vary in sky radiance. For each site, the synop data were used only when doing so does not drop the number of data points to less than 20.

A linear fit of aod against sqm-measured sky radiance was made for each of the subsets of sqm data in each 30-minute bin*. Physically, the slope relates the change in sky radiance with respect to the aod value, whereas the y-intercept can be seen as an extrapolation for the sky radiance without aerosol content.

* Here the units of aod (a unitless logarithmic number) and of the sqm-measured sky radiance (mag_{SQM}/arcsec^2) effectively means that it is a logarithm-logarithm plot, although the aod has a base number of e, and that of mag_{SQM}/arcsec^2 a base number of 10, multiplied by -2.5.

Table 4.3: Summary of night sky observation during the measurement period. The column "Data points" shows the number of minute-by-minute observations during astronomical night (solar elevation angle below −18°) within 15 minutes of local midnight. "WA" shows the predicted clear sky brightness by [14] for sites in North America and Europe. "Clear" and "overcast" indicate the median sky radiance in $\text{mag}_{SQM}/\text{arcsec}^2$ in the respective sky conditions, and the 27th and 81st percentiles for values with an *, indicating lack of cloud coverage data. The brightening factor of overcast sky over clear sky are calculated in linear scale for sites with SYNOP data only. The 22→24 and 24→02 columns show the change in clear sky radiance between the given local times. Sites 46–52 were not included in the main analysis.

N	Site name	Data points	WA	Clear	Overcast	Brightening factor	22 →24	24 →02
1	Tucson KP	358	21.4	21.8*	21.5*	N/A	N/A	N/A
2	Schiermnk	1053	21.3	21.3	21.6	0.7	0.05	0.11
3	Veinto Rg	131	21.1	21.7*	20.9*	N/A	N/A	N/A
4	Tucson Hpk	352	21.3	21.5*	21.2*	N/A	N/A	N/A
5	Winer	1022	21.4	21.6*	21.4*	N/A	N/A	N/A
6	Alice Sp	240	N/A	21.5*	21.5*	N/A	N/A	N/A
7	IP Feld	91	21.3	21.3	21.5	0.9	-0.03	-0.01
8	Tucson Lm	347	20.8	21.3*	20.5*	N/A	N/A	N/A
9	Parey	164	21.3	21.2	21.1	1.1	0.09	0.09
10	Tenerife	2265	N/A	21.3*	20.9*	N/A	N/A	N/A
11	Springendal	1933	20.4	21.1	20.6	1.6	0.10	0.00
12	Rad Kwk	1076	19.9	20.7	20.4	1.7	0.07	0.08
13	Seebergen	758	20.2	20.8	19.3	7.4	0.35	0.07
14	Tucson W	334	19.5	20.4*	18.4*	N/A	N/A	N/A
15	Calgary RAO	5	19.6	20.7*	20.7*	N/A	N/A	N/A
16	Vitto Veneto	300	20.3	20.4*	18.9*	N/A	N/A	N/A
17	Arkemheen	1963	19.9	20.4	19.0	4.5	0.02	0.08
18	CESAR	2009	19.8	20.3	19.1	3.9	-0.03	-0.06
19	Potsdam Bb	2453	19.6	20.2	17.7	13.0	0.03	0.09
20	Arnhem	2115	19.6	20.1	17.9	9.3	0.03	0.11
21	Vestby	167	19.6	20.1	17.9	10.3	-0.15	0.04
22	Lendinara	453	20.3	20.1*	19.3*	N/A	N/A	N/A
23	Berlin Sd	96	19.8	20.0	17.9	8.4	0.04	0.04
24	Tucson N	133	21.4	19.9*	17.8*	N/A	N/A	N/A
25	Grimsby	926	19.4	19.8*	18.2*	N/A	N/A	N/A
26	Met Monte	839	20.0	19.7*	18.1*	N/A	N/A	N/A
27	Castigli	408	20.3	19.8*	18.6*	N/A	N/A	N/A
28	Nove	764	20.0	19.5	17.4	7.5	0.10	0.13
29	Bremen H-L	796	19.3	19.6	17.1	12.0	0.57	-0.04
30	Morehead	575	20.1	19.2	17.2	6.8	N/A	N/A
31	Hamilton	2315	18.9	19.2*	17.0*	N/A	N/A	N/A
32	Berlin St LE	894	18.9	19.1	16.4	13.3	0.29	0.12
33	Berlin St LU	2258	18.9	19.2	16.5	13.5	0.22	0.08
34	Adelaide	1119	N/A	19.2*	16.9*	N/A	N/A	N/A
35	Tucson E	132	18.8	19.2*	17.6*	N/A	N/A	N/A
36	Tucson C	342	18.1	18.6*	16.8*	N/A	N/A	N/A
37	Utrecht	1136	19.1	19.0	16.6	9.2	0.04	0.11
38	Vienna IFA	2272	18.8	19.0*	16.6*	N/A	N/A	N/A
39	Schipluiden	2100	18.2	18.5	15.8	13.8	-0.46	-0.87
40	Plymouth Dv	175	19.5	18.5	15.4	17.6	N/A	N/A
41	Tucson S	130	18.9	18.6*	17.0*	N/A	N/A	N/A
42	Berlin HM	93	18.5	18.3	15.3	16.2	0.20	0.03
43	Madrid UCM	832	17.4	18.1	17.7	1.5	0.20	0.05
44	Edmonton	57	17.2	18.1*	16.3*	N/A	N/A	N/A
45	Vlaardingen	2030	18.7	17.2	16.0	3.2	0.13	-0.25
46	Yonago¶	217	N/A	19.9*	18.6*	N/A	N/A	N/A
47	Mexico¶	434	18.8	18.9*	16.3*	N/A	N/A	N/A
48	Plymouth Rm†	91	20.7	19.0	19.1	0.9	N/A	N/A
49	Plymouth Mk†	38	21.1	19.3	18.6	1.9	N/A	N/A
50	FOA Schöpfl‡	2330	21.0	20.6*	20.3*	N/A	N/A	N/A
51	Deerlick 1§	214	21.3	21.1	20.8	1.3	N/A	N/A
52	Deerlick 2§	3414	21.3	21.3	21.3	1.0	N/A	N/A

¶Window attenuation unknown

†Thresholding problem

‡Instrument failure under dark skies. Later measurements with a properly functioning SQM gave a clear sky radiance of $21.4\,\text{mag}_{SQM}/\text{arcsec}^2$ and an overcast sky radiance of $20.3\,\text{mag}_{SQM}/\text{arcsec}^2$

§Instrument failure

4.5 Results and discussion

THE NIGHT SKY of 2011 and 2012 was found to be ranging in almost four orders of magnitude, or 10 mag$_{SQM}$/arcsec². The darkest first percentile radiance was found at the site Kitt Peak, AZ, USA at 23.24 mag$_{SQM}$/arcsec², and the brightest 99th percentile radiance seen among all sites came from Schipluiden, an area of greenhouses in the Netherlands, at 13.26 mag$_{SQM}$/arcsec².
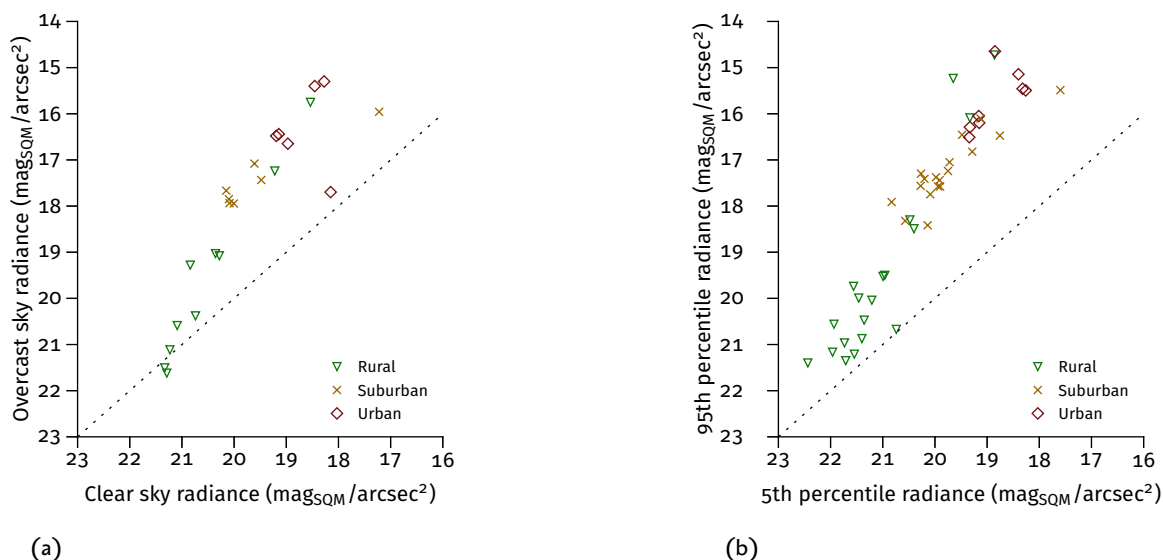

(a)

(b)

Figure 4.5: Comparison of clear to overcast sky radiance. Figure 4.5a shows the median clear and overcast sky radiances for locations where cloud coverage data from weather stations are available, and Figure 4.5b shows the 5th and 95th percentile radiances for all available SQM sites. The dashed line shows the ratio of unity, meaning there is no difference in brightness between cloudy and clear cases for Figure 4.5a, and no variation in sky brightness under different sky conditions for Figure 4.5b [33].

Table 4.4: Variation in sky radiance on clear and cloudy ±15 minutes from midnight. Only sites with SYNOP data for at least six nights both for clear and overcast (8 oktas) cases are included. Values are in mag$_{SQM}$/arcsec² [33]. Sites below the double lines are excluded in the main analysis.

N	Site name	Clear 15.9%	Clear 84.1%	Clear difference	Overcast 15.9%	Overcast 84.1%	Overcast difference
2	IP Feld	21.4	21.2	0.1	21.6	21.4	0.2
9	Parey	21.4	21.1	0.2	21.2	20.9	0.3
11	Springendal	21.2	21.0	0.2	21.0	20.1	0.9
12	Rad Kwk	20.8	20.7	0.1	21.0	19.6	1.4
17	Arkemheen	20.4	20.1	0.3	20.1	18.4	1.8
18	CESAR	20.4	19.8	0.5	19.6	18.5	1.1
19	Potsdam Bb	20.3	20.0	0.3	18.0	17.4	0.6
20	Arnhem	20.2	19.8	0.4	19.1	17.4	1.7
28	Nove	19.7	19.2	0.5	19.0	17.2	1.7
33	Berlin St LU	19.3	19.0	0.3	17.1	16.2	0.9
39	Schipluiden	18.8	18.1	0.7	17.3	14.9	2.4
45	Vlaardingen	17.4	17.0	0.4	16.7	15.5	1.2
52	Deerlick 2	21.5	21.1	0.3	21.9	21.1	0.9

Table 4.3 shows a summary of night sky variations of the participating sites*. For comparison, a pristine, clear night sky typically has a brightness of 21.6–21.4 mag$_{SQM}$/arcsec², and a natural night sky may vary from 24 mag/arcsec² for an overcast sky with thick clouds, to approximately 20 mag/arcsec² when the Milky Way is near the zenith of the sky†. Of the sites with SYNOP data, the darkest median clear sky radiance are found in

* The data from the excluded sites, while also shown in the table, are not considered in all the discussions below.

† Personal communication between C.C.M. Kyba, Deutsches GeoForschungsZentrum, Potsdam, Germany and Dan Duriscoe, National Park Service, USA during preparation of [33].

Schiermonnikoog, the Netherlands (Site 2) and Westhavelland, Germany (Site 7) with a value of 21.3 mag$_{SQM}$/arcsec^2, meaning they are approximately 0.1 mag$_{SQM}$/arcsec^2 (10%) brighter than a night sky not polluted by artificial light, although both sites are many kilometers away from strong night time artificial light sources. It can be said, therefore, that most of the participating sites are light-polluted. Furthermore, 18 sites with SYNOP data have a clear sky radiance brighter than 20.85 mag$_{SQM}$/arcsec^2, two times the natural sky brightness, meaning artificial light is the dominating light source. 30 sites have 95% of time brighter than 20.85 mag$_{SQM}$/arcsec^2. Seven sites (Sites 39–45) situated in suburban, urban, industrial and agricultural areas are more than 10 times as bright as natural sky (brighter than 18.1 mag$_{SQM}$/arcsec^2) 95% of time.

The scatterplots of the median overcast sky radiance against median clear sky radiance, and the 95th percentile sky radiance (brightest 5%) against 5th percentile sky radiance (darkest 5%), are shown in Figures 4.5a and 4.5b respectively. Both figures show a trend in type of site of rural–suburban–urban with increasing sky radiance. The difference between clear and cloudy sky increases with increasing clear sky radiance, but is not in a form of simple power law (like as found in [9]) which would have been shown as a linear relationship in Figure 4.5a, and instead has a change in slope at a clear sky radiance of ca. 20 mag$_{SQM}$/arcsec^2, below of which are all rural or pristine sites. This is in line with the results of a numerical modeling of night sky by Kocifaj and Solano Lamphar [29], which find that the sky the brightening of sky by the presence of clouds increases the nearer to the border of the city, but when an observer moves inside a city the brightening by cloud increases slower with increasing clear sky brightness. Similarly, the difference between the 5th and the 95th percentiles widens as the radiance increases (4.5b). Also notable is that there are two sites with the overcast sky radiance lower than the clear sky radiance, and five sites which are darker than the typical radiance of a natural clear sky radiance, 21.6 mag$_{SQM}$/arcsec^2, 5% of time, which may indicate that they are at least not light-polluted around the zenith, and clouds darken the night sky at these places.

Figures 4.6 shows the density plots of relative frequency of sky radiance against local hour of the night for all the participating sites. The sites are sorted by increasing 5th percentile radiance at the direction of radiance, and the plots are arranged from left to right, top to bottom. The distributions of sky radiance tend to peak at one value for darker sites, whilst brighter sites show bimodal distribution, likely caused by brightening of the sky when clouds are present (also shown in Table 4.4 for sites with more than six nights of clear and overcast sky each). Also noticeable is that for darker sites, there is no significant change in radiance over the course of the night, whereas brighter sites tend to become darker from early evening towards the late midnight (see Figure 4.7 also for histograms for change between 22:00 and 2:00 local time), and for some sites the sky gets brighter again near the dawn. Remarkably, the site in Schipluiden, the Netherlands (Site 39), which is situated around an area with greenhouses switching on their plant lights after the midnight, more than doubles in sky brightness from midnight to 2:00 (Figure 4.7b)*.

* Personal communication with Dorien Lolkema, National Institute for Public Health and the Environment (RIVM), the Netherlands.
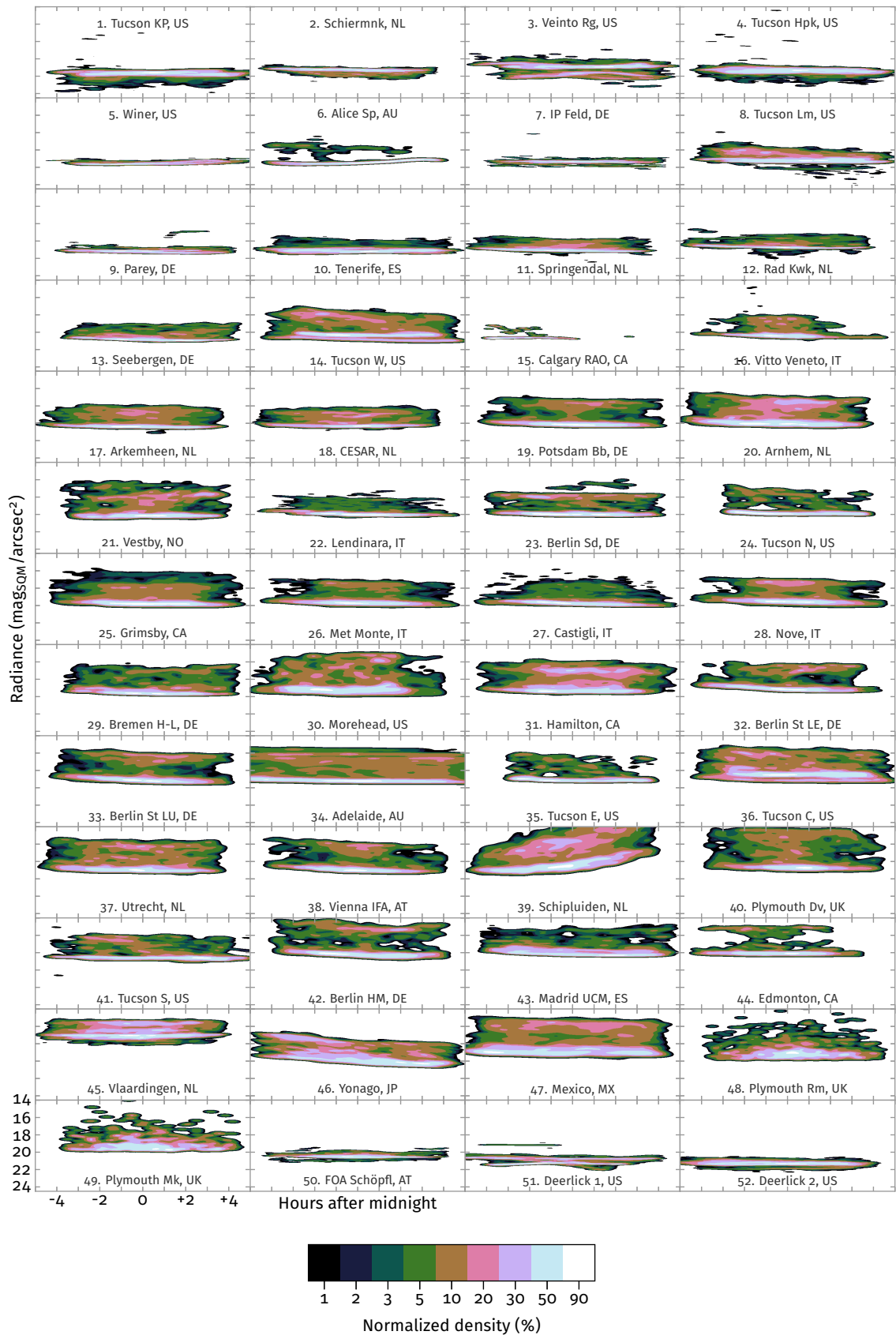
Figure 4.6: Contour plots of night sky radiance for all participating sites. Only measurements taken without astronomical twilight and moonlight were used to generate the composite data. The site number, site name and country code are indicated for each plot. Sites 46 to 52 were not included in the main analysis. Refer to Tables 4.1 and 4.2 for site information [33].
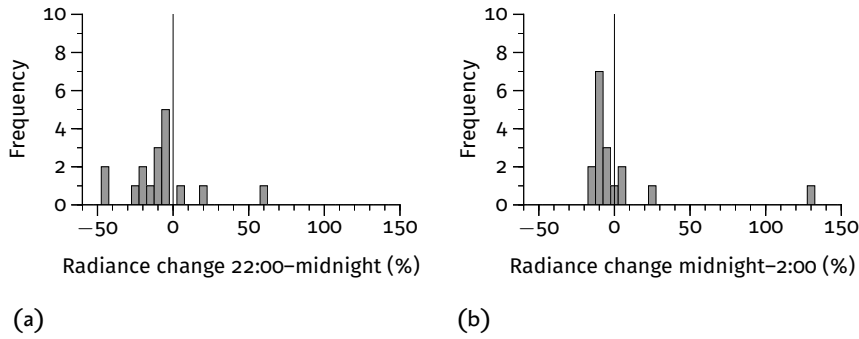
Figure 4.7: Histogram of the observed change in median sky radiance from (a) 22:00 to midnight and (b) midnight to 2:00 on a linear scale. Only sites with synop data and midnight clear sky radiances brighter than $20.85\,\mathrm{mag_{SQM}/arcsec^2}$ (two times the average natural sky brightness) are shown [33].
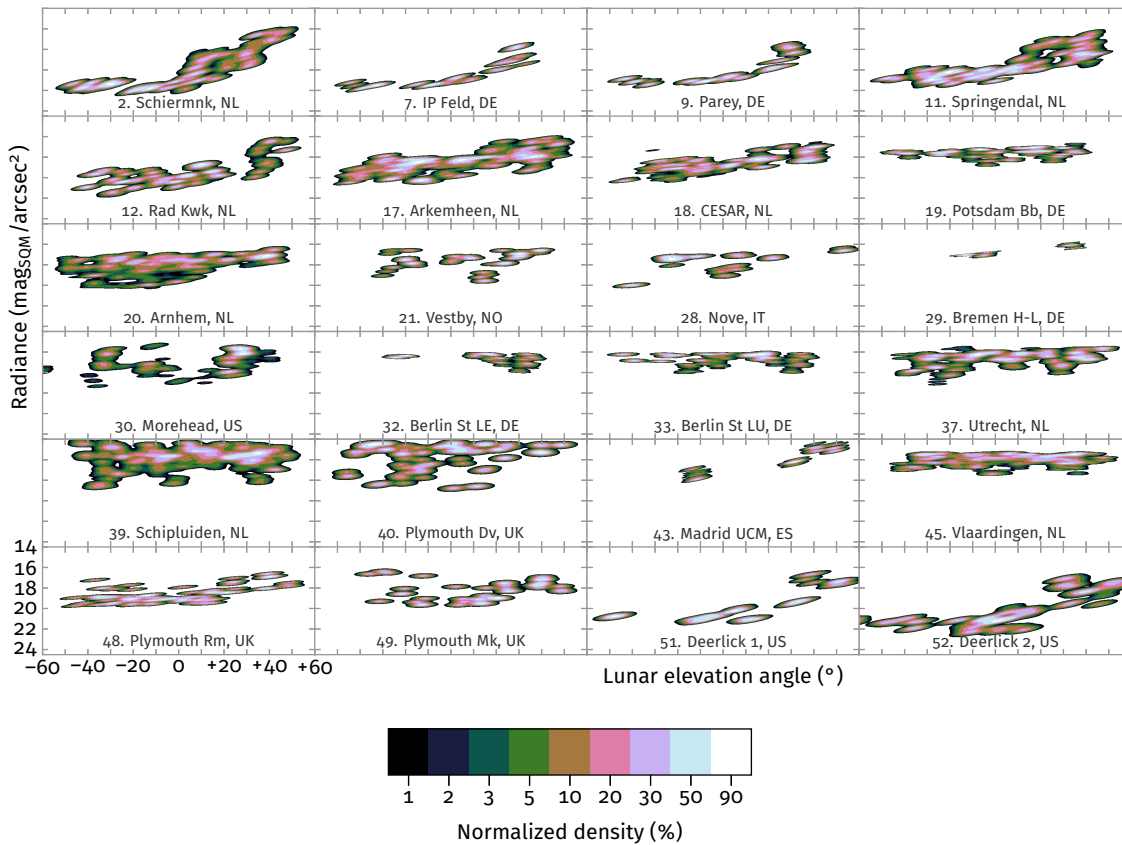

Figure 4.8: Contour plots of cloudy night sky radiance 15 minutes around local midnight at different lunar elevation angles. Only measurements taken with cloud data from weather stations and without astronomical twilight were used to generate the composite data. The site number, site name and country code are indicated for each plot. Sites 46 to 52 were not included in the main analysis. Refer to Tables 4.1 and 4.2 for site information [33].

Table 4.5: Variation in sky radiance on moonlit and moon-free overcast (8 oktas) midnights. Only sites with SYNOP data, at least 40 observations, and data on both moonlit and moon-free nights are included. Values are in mag$_{SQM}$/arcsec^2 [33]. Sites below the double lines are excluded in the main analysis.

N	Site name	Moonless 15.9%	Moonless 84.1%	Moonlit 15.9%	Moonlit 84.1%
2	Schiermnk	21.9	21.3	20.3	17.0
7	IP Feld	21.6	21.4	20.0	17.8
9	Parey	21.2	20.9	20.1	17.9
11	Springendal	21.0	20.1	19.8	17.3
12	Rad Kwk	21.0	19.6	19.9	17.4
17	Arkemheen	20.1	18.4	18.5	17.0
18	CESAR	19.6	18.5	18.5	17.2
19	Potsdam Bb	18.0	17.4	18.0	17.2
20	Arnhem	19.1	17.4	17.8	17.0
21	Vestby	18.2	17.0	18.8	16.7
28	Nove	19.0	17.2	17.4	16.7
29	Bremen H-L	17.1	17.0	16.3	16.1
30	Morehead	17.7	16.1	17.9	15.7
32	Berlin St LE	16.5	16.4	17.2	16.2
33	Berlin St LU	17.1	16.2	17.0	16.2
37	Utrecht	17.8	16.2	17.0	16.0
39	Schipluiden	17.3	14.9	16.2	15.0
40	Plymouth Dv	17.5	14.6	16.5	14.6
43	Madrid UCM	17.9	17.0	16.2	14.8
45	Vlaardingen	16.7	15.5	16.3	15.5
48	Plymouth Rm	19.5	18.8	19.1	17.1
49	Plymouth Mk	19.5	16.7	19.1	17.5
51	Deerlick 1	21.2	20.7	21.0	17.4
52	Deerlick 2	21.9	21.1	20.5	17.5

Table 4.6: Comparison of overcast (8 oktas) sky radiance ±15 minutes around midnight for nights with the moon below and above the horizon. Medians are in mag$_{SQM}$/arcsec^2 [33]. Sites below the double lines are excluded in the main analysis.

| N	Site name	Moonless data points	Median	Moonlit data points	Median	Moon difference
2	Schiermnk	478	21.6	568	18.9	2.7
7	IP Feld	22	21.5	21	19.2	2.3
9	Parey	38	21.1	42	19.1	2.0
11	Springendal	784	20.6	720	18.5	2.1
12	Rad Kwk	440	20.4	369	18.9	1.5
17	Arkemheen	841	19.0	722	18.0	1.0
18	CESAR	591	19.1	680	18.2	0.9
19	Potsdam Bb	399	17.7	420	17.5	0.2
20	Arnhem	1005	17.9	665	17.3	0.6
21	Vestby	21	17.9	46	17.3	0.5
28	Nove	40	17.4	20	17.2	0.2
29	Bremen H-L	60	17.1	30	16.2	0.9
30	Morehead	140	17.2	251	16.2	1.0
32	Berlin St LE	60	16.4	210	16.6	0.1
33	Berlin St LU	285	16.5	330	16.4	0.0
37	Utrecht	351	16.6	422	16.4	0.2
39	Schipluiden	762	15.8	965	15.6	0.2
40	Plymouth Dv	52	15.4	37	15.2	0.2
43	Madrid UCM	30	17.7	90	15.1	2.5
45	Vlaardingen	702	16.0	786	15.8	0.1
48	Plymouth Rm	44	19.1	37	18.4	0.7
49	Plymouth Mk	12	18.6	30	18.2	0.4
51	Deerlick 1	18	20.8	25	19.3	1.5
52	Deerlick 2	382	21.3	408	18.5	2.8
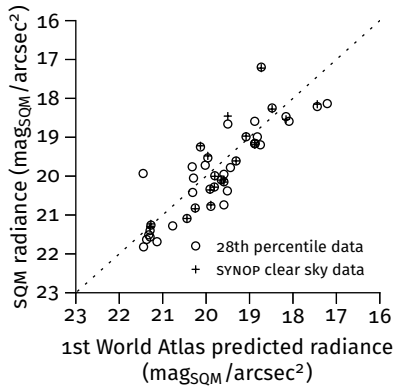
Figure 4.9: Comparison of clear sky observations to values from the First World Atlas of Artificial Light Pollution [14]. Crosses are median clear sky radiance for sites with synop data. If the model fitted perfectly with the observation data, the point would lie on the dash line [33].

While under a natural night sky, a clear, moonless night does not change in brightness throughout the night, the presence of moon can strongly increase the brightness of the sky. Figure 4.8 and Table 4.6 shows how the moon influences the brightness of the sky. In rural or pristine area, the moon is the strongest light source, which can increase the clear night sky radiance by more than 10 times ($2.5\,mag_{SQM}/arcsec^2$). However, in the most light-polluted area, the presence of the moon changes the sky brightness only by less than 20% ($0.2\,mag_{SQM}/arcsec^2$).

4.5.1 Comparison with light pollution model

Figure 4.9 shows a scatterplot of SQM measurement data against the prediction of the First World Atlas of Artificial Light Pollution [14] for clear sky measurements. The model overestimated the sky brightness by about 25%, with a standard deviation of approximately 40%. The difference may be due to the fact that there was snow cover in the satellite data used by the model, and the aerosol content in the atmosphere. In addition, the satellite used for data acquisition, the Defense Meteorological Satellite Program (DMSP), had an overflight time in the early evening.

When the dataset was analyzed, the First World Atlas was the only global light pollution model available. After the publication of [33], Falchi et al. [20] published an updated version of the model using the composite data from the VIIRS–DNB sensor on board the Suomi NPP satellite (Refer to Chapter 3 for details). The model was found to be underestimating by $0.06\,mag/arcsec^2$ (6%), with a standard deviation of $0.46\,mag/arcsec^2$ (+56%,–35%).

4.5.2 Influence of aerosols on sky radiance

Since spatial variation of aerosol can be significant even at a short distance, only colocated stations were used in this analysis. Of all the SQM stations in the campaign, there are only two AERONET stations in vicinity, namely the CESAR in Cabauw (Site 18), the Netherlands, and the campus of the Complutense University of Madrid (Site 43), both at a distance of approximately 200 m. Both sites also have synop data from weather stations, 19 km away for CESAR and 15 km away for Madrid, respectively.

The SQM site in Cabauw is dedicated to atmospheric measurements and research, around 20 km from the city Utrecht and more than 30 km from Rotterdam. Aubé [4] predicted that for a location 20 km away from a city, when the AOD changes from 0.1 to 1.0, the sky brightness is reduced by about one order of magnitude. In practice, however, the sky brightness can vary greatly due to both the meteorological conditions inside and outside of the city. As a result there is no consistent relationship between the AOD and the SQM radiance (Figure 4.10): the slope varies between $-2.7\,mag_{SQM}/arcsec^2/AOD$ and $+3.9\,mag_{SQM}/arcsec^2/AOD$, and the correlation coefficient ranges from -0.98 to $+0.99$.

The SQM site in Madrid, situated approximately 4 km from the city center, and 7 km from the brightest place in Madrid [6], has a more consistent relationship between the measured night sky radiance and the AERONET AOD (Figure 4.11). Although there is a drop in slope at 1:30, there is a consistent amplification of sky radiance with increasing aerosol content. It

(a) Radiance vs. AOD   (b) Fit parameters vs. time of night
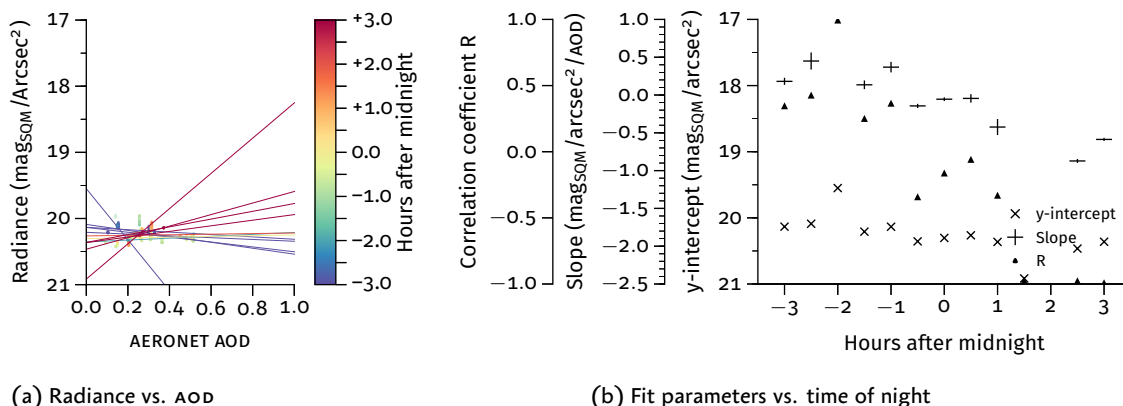
Figure 4.10: Relationship between AERONET AOD and SQM-measured sky radiance in Cabauw, the Netherlands (Site 18). Figure 4.10a shows the individual data points and linear fits color-coded with local hours of the night, and Figure 4.10b shows the fit parameters with the correlation coefficient. Only data points with available cloud coverage data was used to generate the plots, and the standard deviation for each included night must be smaller than $0.14\,\mathrm{mag_{SQM}/arcsec^2}$ to further screen out nights under changing meteorological conditions. A *negative* value in slope means an *increase* in radiance with increasing AOD.

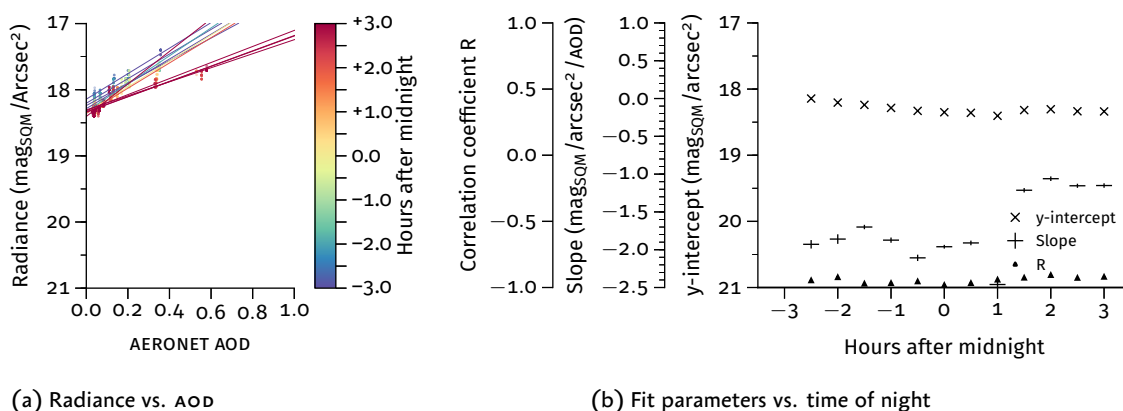(a) Radiance vs. AOD   (b) Fit parameters vs. time of night

Figure 4.11: Relationship between AERONET AOD and SQM-measured sky radiance in Madrid, Spain (Site 43) using the same data analysis and visualization schemes as Figure 4.10.

is notable, however, that while [4] predicted no or little amplification of sky brightness when the AOD increases from 0.1 to 1.0 5 km away from the center of light source, the factor of amplification in Madrid is always higher than $1\,\mathrm{mag_{SQM}/arcsec^2}$ when the AOD increases by 1.0. This may be due to the fact that the SQM is a broadband radiometer, whilst Aubé's calculation was based on a wavelength of 569 nm.

4.6   Summary

THIS STUDY was the first coordinated effort to use automated radiometers to quantify the worldwide variation of sky brightness. It shows how the introduction of artificial light at night changes the natural night sky patterns. Inside and near populated areas, the variation of night sky no longer follows the natural pattern dominated by the presence of the moon, but instead by the meteorological conditions, for example the cloud coverage and the amount of aerosols present, and instead of darkening, cloud-covered sky

becomes brighter. As shown in Chapter 1, this may change the predator–prey balance, and can disorient night-flying migratory birds.

However, as this study only covered mostly the Western Hemisphere in developed countries, it is still not representative for the night sky scenarios of the whole world. Moreover, the study period of two years is not sufficient for investigating long-term changes in night sky brightness, which can be influenced by changes in human behavior, lighting technology and urban planning. For all these reasons, it is necessary to continue monitoring the night sky, either by satellite or ground-based observations — which will be studied in the next chapter.

5 Long-term ground-based night sky monitoring in and around Bremen

PREVIOUS SURVEYS suggest that in average, cities in Europe brighten up at a rate of approximately 5 % per year [23]. As a result of recent technological advances and cost reduction, as well as increase in energy efficiency, in solid state lighting, for example light-emitting diode (LED) and potentially laser diode lighting, which typically emits a larger fraction of blue light than existing lighting technologies and the pressure in reducing carbon emission, Europe may experience enormous change in lighting pattern, which may lead to higher level of light pollution and disrupt circadian rhythm of human beings [66].

To assess the impact of technological and behaviorial change in lighting and use of artificial light, it is necessary to monitor the night sky over a long period. This can be either achieved by satellite-based (Chapter 3, or see [23]) or ground-based (Chapter 4) measurements.

5.1 Rationales for long-term night sky monitoring in Bremen

THE CITY OF BREMEN, situated in Northern Germany surrounded by the federal state of Lower Saxony, is the tenth largest city in terms of population, and the fifth largest in terms of area.

Built along the Weser River, Bremen is a typical European medium-sized city, with land uses ranging from heavy industries and logistics, to parks and natural reserves. Topographically Bremen is a flat city with an elevation of 10.5 m above mean sea level at the marketplace of the city center, and a maximum natural elevation of 32.5 m, the lowest among all states within Germany [21].

The public lighting system of Bremen consists mainly of a mixture of florescent lights for low-power, small-area uses, and high-pressure-sodium (HPS) lights when high output power is necessary. Since ca. 2013, new installations of public lighting systems involve the use of white LEDs, an example of which is shown in Figure 5.1. Some of the fixtures with compact florescent lights are also being retrofitted with LED modules.

Before commissioning Bremen's long-term SQM measurements in December, 2011, some individuals measured the night sky of Bremen using naked eye or handheld SQMs and put the results online. Since its introduction in 2013, the Loss of the Night mobile app collects several dozens of single point measurements each year. However, this effort is not coordinated. In addition, using the annual Defense Meteorological Satellite Program (DMSP) composite data Hänel found a slight decrease in upwelling radiance for Bremen and some other places [23] without further investigation. The measurement at the campus of the University of Bremen and in the village Seebergen in Lilienthal, Lower Saxony is the first long-term ground-based measurement and experimental study of light pollution in Bremen.
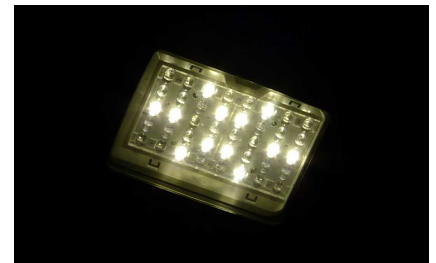

Figure 5.1: LED modules inside a fixture of street lamp near the campus of the University of Bremen. Note that only 12 out of 40 modules are lit to reduce the output power of the street lamp.

The gradual change of lighting technology from HPS and compact florescent lighting to solid-state lighting, for example LEDs, provides an opportunity to identify the impact on skyglow by means of long-term measurements.

5.2   Night sky monitoring by SQMs

Since December, 2011, an SQM-LE was installed on the roof of the U-Building of the Faculty of Physics and Electronics of the University of Bremen in the district Horn–Lehe (Bremen H–L, Site 29 in Chapter 4), continuously measuring the zenith night sky radiance. Characteristics of the SQM are shown in the last chapter. There are some exterior lightings used at the Universum Bremen (a science museum) and at the drop tower approximately 900 m away from the measurement site, however these light sources are not directed to the site and considering the sensitivity of the SQM near the horizon, no effect is expected on the measured radiance. Moreover, no direct light sources are present at the site during night time. Another SQM was set up in late February, 2012 outside a family house in the village Seebergen near Lilienthal, Lower Saxony (Seebergen, Site 13 in Chapter 4) which is directly at the border of the state of Bremen to find out the difference in skyglow pattern between a suburban site and a rural site. Through internet connection data is directly acquired by and saved to the data server of the working group. Both SQMs report zenith sky radiance once per minute.

The Bremen City Airport, situated approximately 7.4 km from the suburban site and 16.1 km from the rural site, hosts a World Meteorological Organization (WMO) weather station with index number 10224. The weather station reports hourly by a human observer, with some gaps of observations sometimes happening at 21:00 and 2:00 UTC each night.

To ensure that the attenuation of the glass windows for both of the devices do not change significantly during the whole measurement period, the glass windows are inspected regularly (once per day except weekends for the campus site, once per week for the rural site). The glass windows are wiped clean when they are found to be dirty, for example with deposits of aerosols. If bird droppings are found, data points between inspections are removed from the analysis. Also, when the silicone sealing is found to be aged and not more watertight, the glass windows are resealed.

During the initial months of measurements, an inter-comparison was done with the two devices used in Bremen, the results of which can be found in [62]. With help of a calibration box and the same procedure of operation as shown in [62], the SQMs are removed each year to check for the attenuation values of the housing (Table 5.2). In [49] Pravettoni found out that some glass windows were visibly yellowed, possibly due to exposure to solar ultraviolet (UV) radiation. However, apart from aging of the sealant as mentioned above, aging of the windows themselves are not seen from naked eye. Moreover, fluctuations of the attenuation values for the glass windows we use in this study are within the manufacturer's stated uncertainty of the SQM. We therefore consider the glass windows' attenuation values to be stable in this analysis, and the constant assigned in

Table 5.1: List of Bremen night sky monitoring sites.

Site	Bremen H–L	Seebergen
Latitude (°)	53.1038	53.1363
Longitude (°)	8.8498	8.9851
Elevation (m)	22	11

Table 5.2: Attenuation value of SQM housings' glass window. Values are in $mag_{SQM}/arcsec^2$.

Date	Bremen H–L	Seebergen
2012	0.108±0.004	0.094±0.047
2013	0.149±0.003	0.111±0.004
2014	0.110±0.003	0.105±0.005
2015	0.100±0.000	0.108±0.005
2016	0.120±0.002	0.106±0.005

[62] are used throughout the whole period.

We encountered several instrument issues during the measurement period. Starting from July 2012, the device for the rural site experienced a lag in reporting the data by one request, and was subsequently replaced with another unit by the manufacturer in summer 2013. The instruments also suffer from aging of the lenses (Figure 5.2), possibly due to exposure to sunlight. The rate of decrease in sensitivity due to this, however, could not be determined because there was no light source for absolute calibration available*. In addition, some sources of lighting, for example skybeamers, can be seen if the light path passes near the zenith of the sqm. Correspondingly, these data points are excluded when finding the long-term trend.

5.3 Narrow field-of-view cooled CCD spectrometer

Although the sqm is also sensitive to shorter wavelengths, it cannot detect the relative change to other wavelengths as it is a broadband radiometer. Simultaneous measurements of the sqm and a spectrometer capable of measuring light of shorter wavelength enables the detection of the relative change in blue emission to the whole visible spectrum of the skyglow.

A CCD spectrometer, which is mainly used for measuring trace gases in the troposphere and stratosphere using the differential optical absorption spectroscopy (DOAS) technique by the DOAS Group at the Institute of Environmental Physics, is also used for nighttime measurements since August 2012[†]. The spectrometer uses a 2D cooled CCD and a Czerny–Turner monochromator, and has a telescopic objective lens with an equivalent focal length of 275 mm and a field of view of about 2°, pointing towards the zenith.

Sensitive to uv and visible light of shorter wavelengths, we use the CCD spectrometer to observe the night sky at the zenith at the wavelengths of 435.8 nm±2.125 nm and 452 nm±5.95 nm with a resolution of 0.085 nm. 435.8 nm is one of the emission lines for mercury, usually originating from florescent lights or mercury lights, and is also near the peak emission line of commercially available blue or white LEDs at 430 to 450 nm. For these reasons this line is chosen. The measurements at 452 nm were analyzed initially, but not subsequently used because the noise level is higher than the 435.8 nm line, possibly due to wider line width and lower signal. As an instrument used for teaching and for daytime measurements, it is not radiometrically calibrated for use at night, and as a result of not having a calibration source in the dynamic range of the night sky brightness, it is not possible for the time being to compare the readings with the sqm, and the data are presented in units of raw counts per second, with the noise floor of the sensor subtracted to give out net count rates.

The CCD sensor of the spectrometer is known to pick up spikes in measured values due to cosmic radiation, although the exact cause is not known[‡]. The original dataset comes with data either removed or compensated. However some data points are overcompensated and register as low counts instead, and can only be seen when plotting the data against those taken by the sqm. This means there must be simultaneous sqm measurements to validate whether the raw readings are affected by overcom-

Figure 5.2: Aging of sqm plastic lens due to exposure to sunlight. Note the slightly yellowish color.

* From the raw data of glass attenuation measurement, the reading of the sqms have dropped in the order of 0.15 mag$_{SQM}$/arcsec^2 over the span of four years, implying an annual degradation rate of roughly 0.04 mag$_{SQM}$/arcsec^2. However, the geometry of the setup, as well as the output of the light source, which is an incandescent lamp, are not calibrated.

† The instrument used for this study now serves mainly for teaching purpose. More details about the improved version of the instrument which can measure at different zenith and azimuth angles can be found at [48].

‡ Personal communications with Andreas Richter, University of Bremen, 2016.

(a) Before amplifier replacement   (b) After amplifier replacement
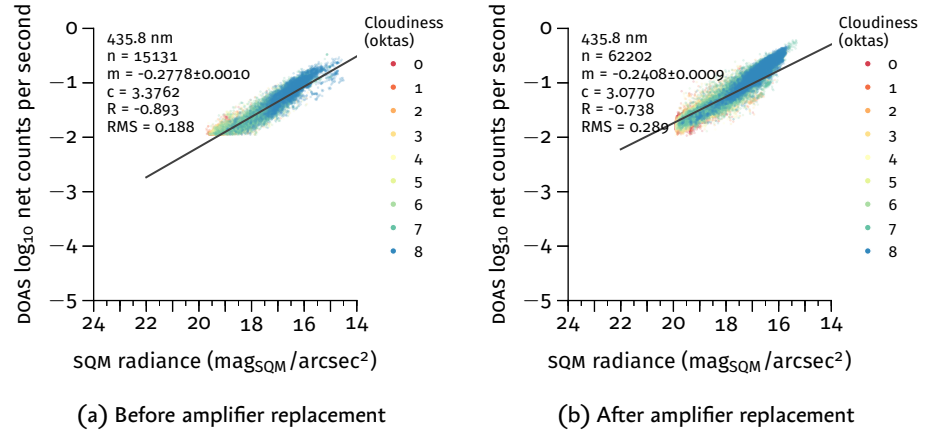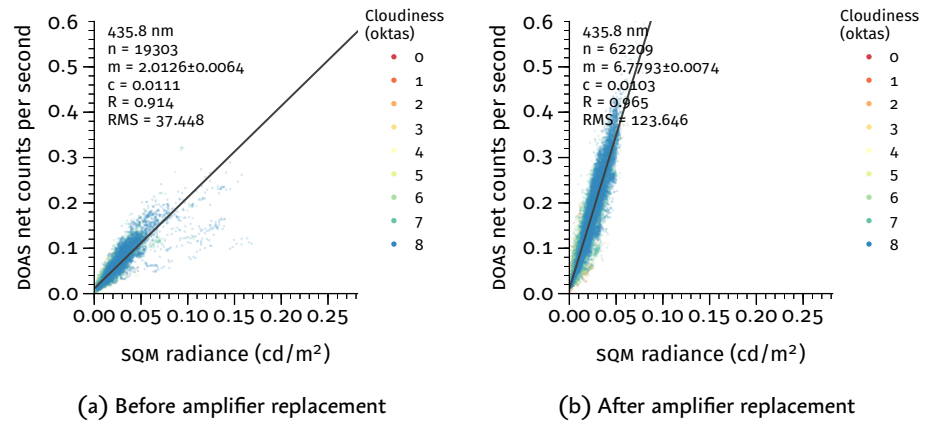
Figure 5.3: Scatterplots of measured count rate of the cooled CCD spectrometer against SQM radiance before linear offset and gain corrections. Only data with cloud coverage information are used. Count rate of the cooled CCD measurements is in logarithmic scale. Figure 5.3a shows the data point before the replacement of the amplifier in late February, 2014, whereas Figure 5.3b shows those thereafter. Data points which are farther than 2 RMS values away from the fit are not included.

(a) Before amplifier replacement   (b) After amplifier replacement

Figure 5.4: Scatterplots of measured count rate of the cooled CCD spectrometer against SQM radiance before linear offset and gain corrections in linear scale, with the same dataset in Figure 5.3, but with the SQM-measured radiance converted to linear scale in the unit of cd/m².

pensation. In March, 2014, the signal amplifier module of the instrument was replaced to improve the signal-to-noise ratio. The count rate of the instrument has changed correspondingly since then. Figures 5.3a and 5.3b show the logarithmic count rate of the CCD spectrometer against the SQM measured radiance for data before and after the change of amplifier, effectively a logarithm–logarithm plot because mag_{SQM}/arcsec² is a unit in logarithmic scale. Also, because of the multiplication factor of -2.5 used by the definition of the astronomical magnitude, a strictly linear relationship yields a slope of -0.4 instead of unity. Figure 5.4 shows the same scatterplot in linear scale converted to the unit of cd/m² by the factor

$$1.08 \cdot 10^5 \cdot 10^{-0.4 \cdot L_{SQM}}$$

(a) Before amplifier replacement
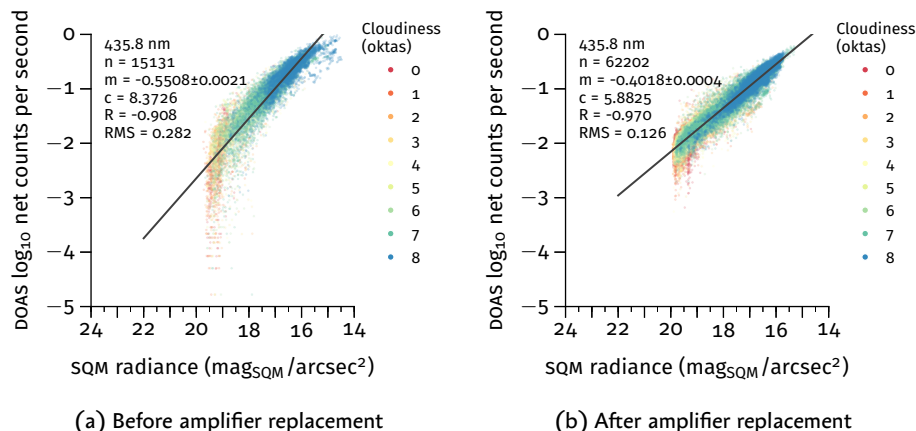
(b) After amplifier replacement

Figure 5.5: Scatterplots of measured count rate of the cooled CCD spectrometer against SQM radiance after linear offset and gain corrections, using the same visualization scheme.

where L_{SQM} is the SQM-measured radiance in $mag_{SQM}/arcsec^2$ *. With the linear fit of the CCD spectrometer raw count rate against SQM radiance converted to linear scale, the linearity and the linear offset of the sensor can be found. With the data points first filtered by excluding points outside of 2 root-mean-square (RMS) deviations from the logarithmic fit to account for over and under-compensation of spikes, and then compensated for the linear offset, data points taken before the amplifier replacement are linearly scaled to match the fitted slope of those after the replacement. The two subsets of data are then treated as one continuous dataset. Figures 5.5a and 5.5b show the logarithm–logarithm plots before and after the amplifier replacement respectively. Overall, the resulting scatterplots show a more linear relationship between the spectrometer and the SQM readings, as shown by the slope of the fit in logarithmic scale being close to the expected value of –0.4. However, as a result of operations in linear scale, the lower readings from the measurements using the old amplifier reveal higher degree of nonlinearity than those using the new amplifier when plotted in logarithm–logarithm scale.

* Found in the website of Unihedron, the SQM's manufacturer at http://unihedron.com/projects/darksky/magconv.php. However this conversion is approximate as the spectrum of skyglow tend to shift towards the red regime as the brightness increases. See for example [32].

5.4   Results and discussion

5.4.1   *Variation of sky brightness during the course of night*

(a) Bremen H–L   (b) Seebergen
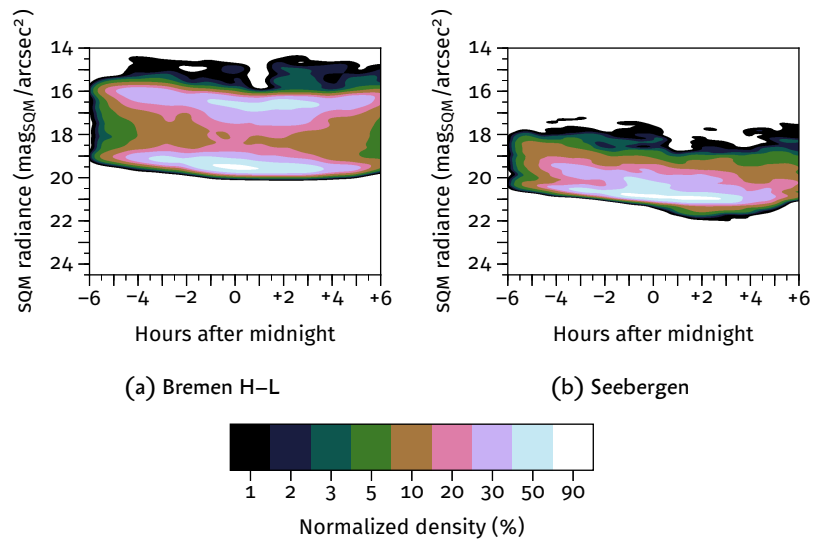
Figure 5.6: Contour plots for sqm measurements at the two measurement sites in Bremen. Similar methodology as in Chapter 4 is used, and the plotting scheme is the same as Figure 4.6. Only data taken without astronomical twilight and moonlight are shown here. In addition, data points are not used when snow cover is reported at the weather station in Bremen City Airport.

(a) Bremen H–L   (b) Seebergen
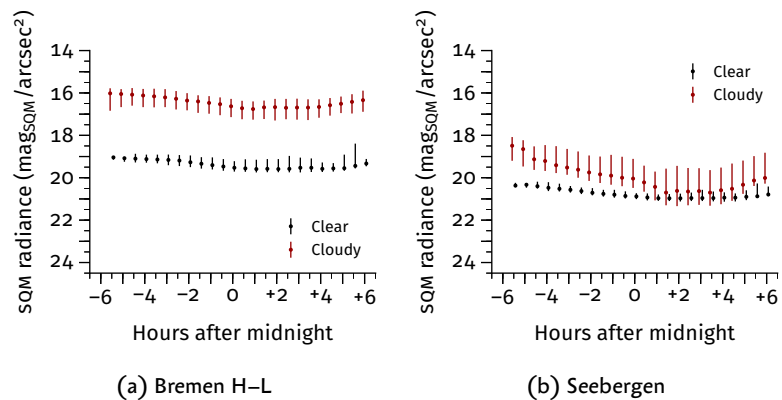
Figure 5.7: Median night sky radiance at different hours of night in Bremen. Only measurements taken without twilight and moonlight, and with cloud coverage data from weather station are used to generate these plots. Error bars are values at $\pm 1\sigma$.

THE DISTRIBUTION in sky radiance of the suburban site (Figure 5.6a) is found to be different from that of the rural site (Figure 5.6b). For the suburban site, a bimodal distribution is noticeable throughout the course of the night, typical for light-polluted areas due to backscattering of artificial light with and without clouds. The lower band corresponds to the scenario of clear sky, whereas the upper band corresponds to the cloudy scenario. For the rural site (Figure 5.6b), however, the radiances are 1 to 2 mag$_{SQM}$/arcsec^2 smaller, and they decrease during the course of the night stronger than

the suburban site. Moreover, the bimodal distribution is only discernible during the early hours of the night, and vanishes and becomes a unimodal distribution around the midnight. A further drop in sky radiance can also be seen at around 1:00. Also, the spread of sky radiance of the rural site is lower than that of the suburban site. Most of the data points are concentrated around the midnight because the data points taken with astronomical twilight and moonlight are not used, and the solar elevation angle in Bremen is the lowest around the local midnight.

Although the weather station in Bremen is not in the vicinity of both of the measurement sites, the cloud coverage data from the weather station can still give insights of the relationship between the presence of clouds and change of sky brightness, as well as the effect of distance of major light sources/light dome of the city. The midnight clear sky radiance of the suburban site is $19.53^{+0.38}_{-0.31}$ mag$_{SQM}$/arcsec², whilst the overcast sky radiance is $16.63^{+0.51}_{-0.35}$ mag$_{SQM}$/arcsec². The overcast sky was thus brighter by a factor of 14.45. The night sky of the rural site, on the other hand, has a median radiance of $20.88^{+0.13}_{-0.15}$ mag$_{SQM}$/arcsec² for clear nights and $20.04^{+0.44}_{-0.93}$ mag$_{SQM}$/arcsec² for overcast nights, yielding a ratio of 2.17 between the radiances of clear and overcast sky (Figure 5.7b). This is in line with the findings in Chapter 4 that the brightening ratio of the night sky increases with clear sky radiance. As there are only two sites available in Bremen, whether a break in the slope of overcast sky radiance with respect to clear sky radiance demonstrated in Chapter 4 cannot be directly verified.

Also as already shown in Chapter 4 a decrease in sky radiance in the progress of the night can also be seen both under clear and overcast sky, with an observed increase again towards the morning hours. For the suburban site the clear sky radiance drops from 19.04 mag$_{SQM}$/arcsec² at 18:30 local time to 19.59 mag$_{SQM}$/arcsec² at 1:00, a decrease of approximately 40%, and the decrease in sky radiance in the same interval when the sky is overcast is approximately 50%, from 16.02 mag$_{SQM}$/arcsec² to 16.76 mag$_{SQM}$/arcsec². The corresponding brightening factor by the presence of clouds decreases from 16.14 to 13.55. For the rural site, while the clear sky darkens from 20.33 mag$_{SQM}$/arcsec² at 19:00 to 20.97 mag$_{SQM}$/arcsec² at 1:30–2:30 (a decrease of 45%), the overcast sky radiance decreases from 18.49 mag$_{SQM}$/arcsec² at 18:30 to 20.70 mag$_{SQM}$/arcsec² at 1:30, a decrease of 87%. Also notable is the difference between the maximum and minimum brightening factors for the two sites: whilst that of the suburban site varies between 13.55 and 16.29, the brightening factor of the rural site can vary between 1.27 and 5.65. Such a difference in the darkening of a clear sky and overcast sky may possibly be attributed to the curfew of the public lighting at 1:00 local time[*]. During the hours which the brightening factor is around the minimum, i.e. for 1 a.m. to 4 a.m., the $+1\sigma$ overcast sky radiance (i.e. the 15.9th percentile radiance value) is darker than the $+1\sigma$ clear sky radiance, indicating that the sky may be *darkened* by clouds covering the sky in the hours after the midnight, depending on the cloud properties such as the droplet size and cloud base height.

[*] Personal communication with Christine Weinzierl, Institute of Environmental Physics, University of Bremen.
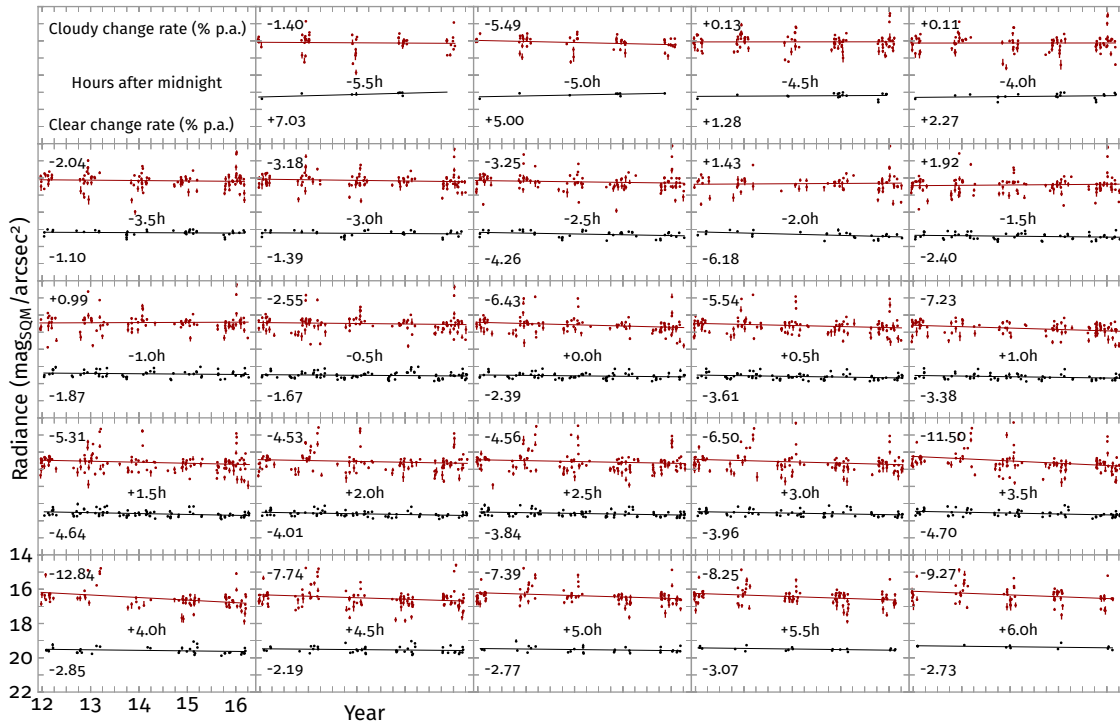
(a) Bremen H–L
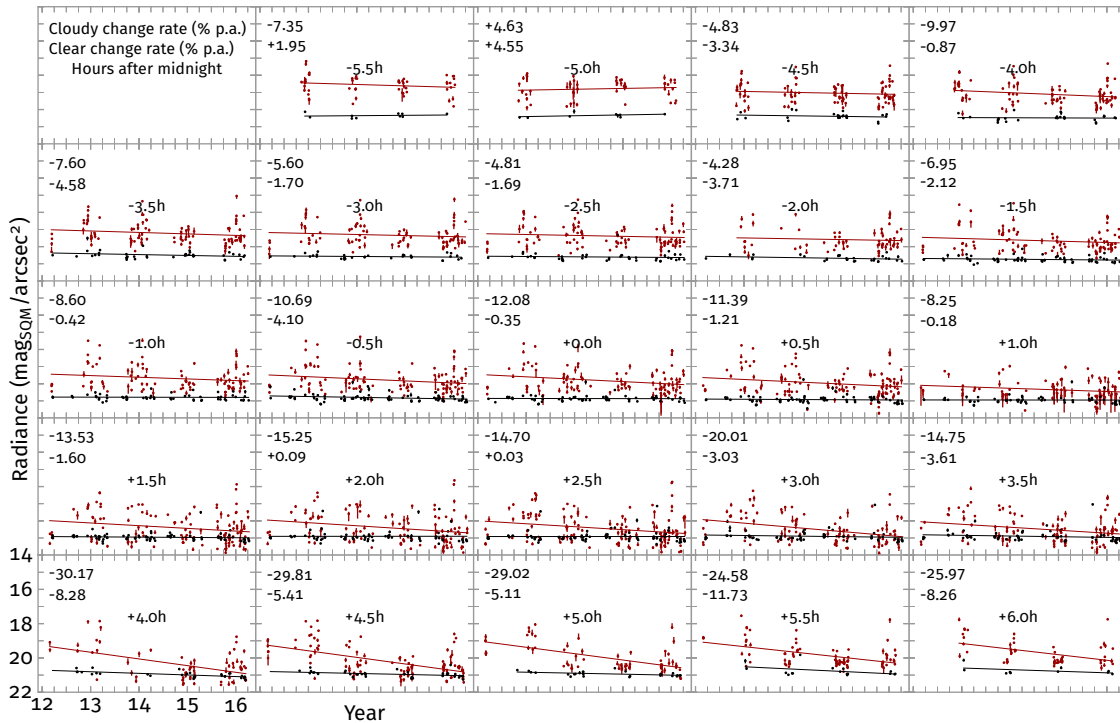
(b) Seebergen

Figure 5.8: Time series of daily median sky brightness at different hours of night. Only measurements taken with weather data are used. Measurements made during overcast nights are in red, whereas those taken during clear nights are in black. Thresholds in daily variation are used as an extra measure for weather screening. Error bars are values at $\pm 1\sigma$. The lines are logarithmic fits of the time series, with the fitted annual change rates indicated.
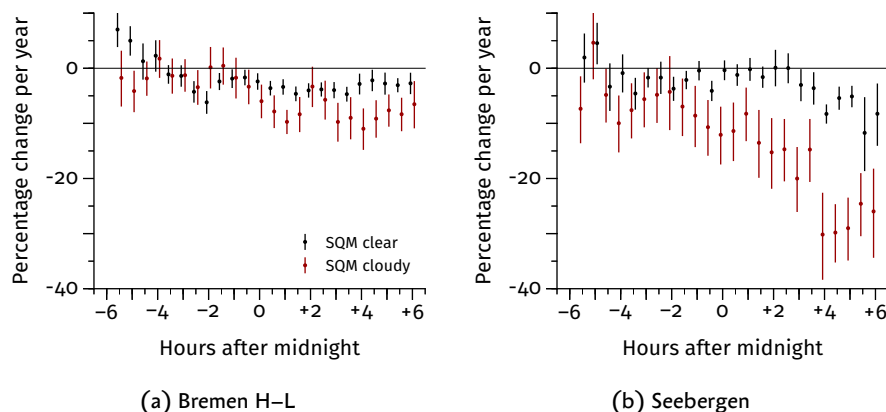
Figure 5.9: Fitted rate of change of sky brightness for the suburban and rural sites in Bremen. Data for overcast sky is in red, and data for clear sky is in black.

5.4.2 Change of sky brightness over the measurement period

DURING THE COURSE of the measurement period, changes in clear and overcast sky radiances could be observed. For the suburban site, there is an increase of clear sky radiance for the early hours of the night over the measurement period of ca. 4.5 years, and the change in cloudy sky radiance is statistically not significant, partly due to the larger variation of sky brightness associated with cloud properties. However, the sky radiance from midnight and on are consistently decreasing, with the clear sky radiance decreasing at an annual rate of 2 to 4%, and the annual rate of decrease for cloudy night ranging from 5 to 12% (Figure 5.8a). For the rural site, the clear sky radiance remained statistically constant or decreased slightly for most of the night during the measurement period, with an extreme values of annual rate of change at −11.7% and +4.6%. The annual rate of change for the overcast sky radiance, like in the suburban site, show a decrease for most of the hours of the night. Noticeable is that the annual rate of decrease is higher than that for the suburban site — 13 out of the 24 available 30-minute periods have an annual rate of change <−10%, mostly concentrated during the later part of the night (Figure 5.8b). A summary of annual rate of change for both sites can be found in Figure 5.9.

During a site visit in early December, 2016 the following notable features at and around the rural site were found:

- There are two trees within 20 m from the SQM, which have been growing throughout the measurement period. While they are situated in the direction to Bremen from the SQM which can potentially block the skyglow from entering the optical path of the SQM, they are outside of the FWHM field-of-view of the SQM, and the effect of blocking by these trees may be considered insignificant.
- A number of trees were removed on a knoll near the site. Since trees typically have lower reflectance relative to the bare soil or land for agricultural uses, especially for shorter wavelength of the visible spectrum [18], it is unlikely that the removal of the trees caused the decrease in sky brightness.

- Villages around Seebergen are sparse, and public lighting for the major roads outside the village are less concentrated than those inside the village. Seebergen can therefore be considered as a localized light dome.
- Majority of street lamps in Seebergen are cool white florescent light without cutoff above the horizon, which may increase the local sky glow due to the rich blue content in the emission spectrum.

The observed decrease of brightness due to degradation of the optical system, a shift of the emission spectrum of the artificial light at night to lower wavelength because of the switch of public lighting to LEDs, cannot be positively ruled out. On the other hand, taken the observations above into account, the non-linear relationship between the decrease of clear sky radiance to cloudy sky radiance (i.e. the larger slope for the change in overcast sky radiance than that in clear sky radiance), which have already been shown in Chapter 4, Figure 4.5a, may indicate that the night sky has physically darkened. Existing lighting systems which are not yet replaced may decrease their output power during their life spans. The switch to LED lightings are underway only progressively in Bremen as of this writing, and all lightings of existing technologies do decrease their output before their eventual replacement [53]*. This may result in an overall decrease in emission if the lifetime of the new LEDs is much longer than the observing period and the introduction of LEDs just started at the beginning of the observation period. The decrease is more noticeable during the later part of the night: many domestic and commercial lightings are switched off during the course of the night, while within the city of Bremen, there is no curfew for the public lightings, meaning that the *relative* contribution of the public lighting to the skyglow is higher at later in the night. For the rural site, the higher rate of decrease of overcast sky radiance is an expected result, when the output of the lighting systems in the city and the surrounding have decreased. While there is no behavioral change in the use of domestic lighting, and that the curfew of public lighting has been in place since the begin of the measurement period, these factors may be ruled out.

* This includes LEDs after an extended period of use. Some manufacturers program their LED modules to increase the power in order to compensate the decrease of output during the lifetime (personal information gathering from a sales representative during the 3rd International Conference on Artificial Light at Night, 2015, Sherbrooke, Canada).

5.4.3   *Measurements with cooled CCD spectrometer*

A density plot of the measurements made by the CCD spectrometer with respect to the hours of midnight is shown in Figure 5.10a, and the median clear and overcast sky radiance for different time of the night in Figure 5.10b. In comparison to the SQM measurements (Figure 5.6), both show a more pronounced bimodal distribution in count rates throughout the night, with a drop in count rate over the course of the night. However, the time series over different hours of night (Figure 5.11) shows that the measurements taken before the replacement of the amplifier in March 2014 varied more than those taken thereafter, indicating that the noise level of the device during clear sky is too high for quantitative measurements. Also, although a similar decreasing trend of count rate can be seen for overcast nights, some sources of systematic uncertainties, none of which has been quantified, must be taken into account. First, the glass window of the device has not been cleaned during the measurement period, and the effect of accumulating deposit is to be known. Second, the alignment was found to have been

(a) Density plot

(b) Overcast/clear median count rates
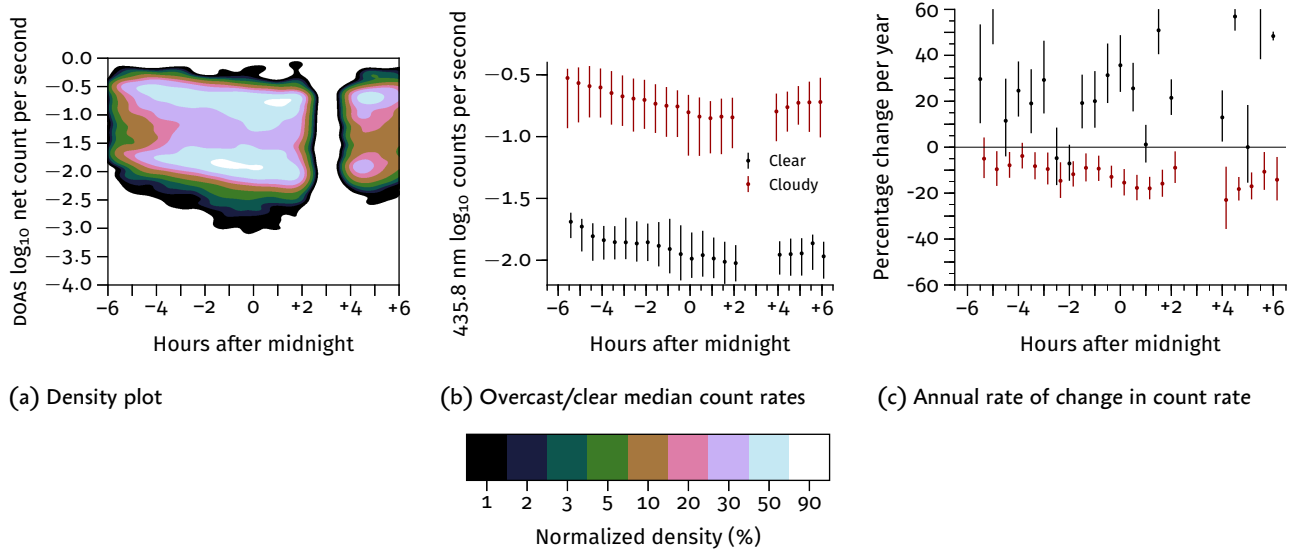
(c) Annual rate of change in count rate

Figure 5.10: Summary of long-term measurements using the cooled CCD camera at 435.8 nm. Only measurements taken with weather data and simultaneous SQM measurements are used. The count rate is corrected for linear offset and gain using the method described in Section 5.3 for offset and difference in gain in amplifier for data taken before March, 2014. The y-axes of all plots are in logarithmic scale. Error bars in Figure 5.10c indicate values at $\pm 1\sigma$.
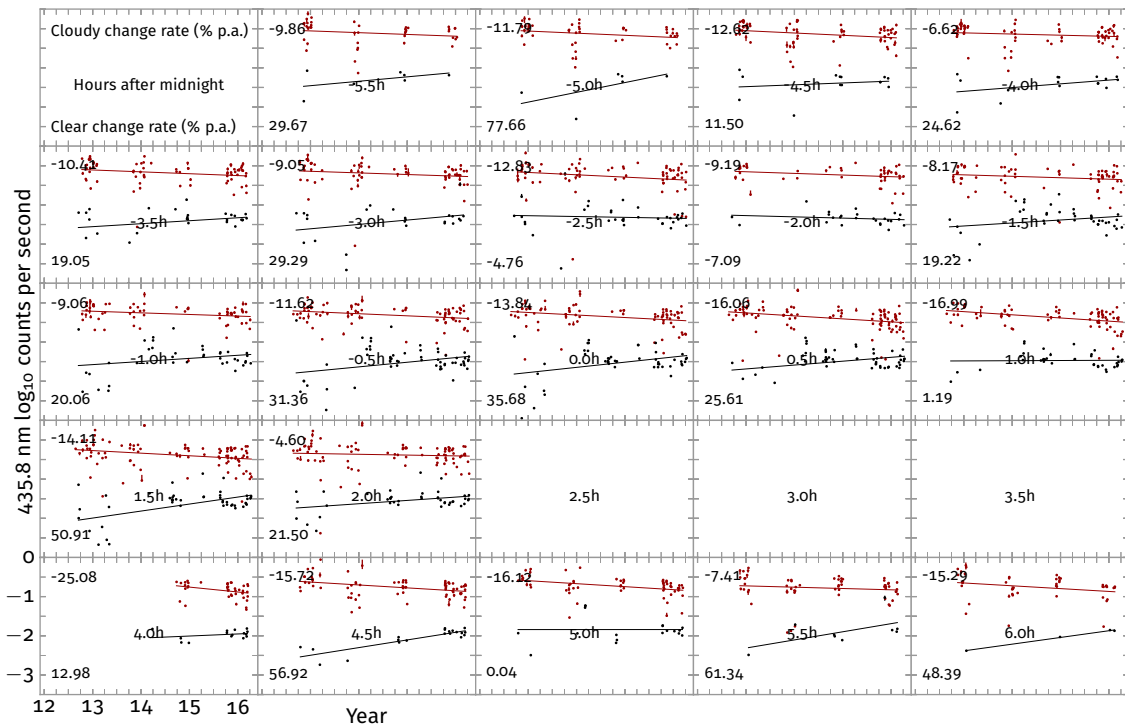

Figure 5.11: Time series of daily median sky brightness at different hours of night at 435.8 nm using the cooled CCD spectrometer. The y-axis is in logarithmic scale. Only measurements taken with weather data and simultaneous SQM measurements are used. The count rate is corrected using the method described in Section 5.3 for offset and difference in gain in amplifier for data taken before March, 2014. Measurements made during overcast nights are in red, whereas those taken during clear nights are in black. Thresholds in daily variation are used as an extra measure for weather screening. Error bars are values at $\pm 1\sigma$. The lines are logarithmic fits of the time series, with the fitted annual change rates indicated.

changed during the inspection in November, 2016. Third, the sensor has not been checked for its degradation in sensitivity. Therefore, while a clear relationship between cloud coverage and count rate can be seen from the dataset, radiometric calibration and sensitivity check must be done in the future in order to quantify changes of night sky brightness at particular wavelengths.

5.5   Summary

Based on the ground-based measurements spanning over 4.5 years, we are able to monitor how the night sky changes within a night, and how it evolves in the course of the measurement period. While we were not yet able to quantify the spectral change with the gradual replacement of public lighting to LED-based system due to lack of instrument, we observed a general decrease of night sky brightness in and around the city of Bremen. I suspect, however, that this is by no means a result by the introduction of a more sustainable urban lighting plan. Rather, it is a result of the slow rate of replacement of public lighting to newer technologies. As I observed that the replacement is still ongoing in and around the city, we need to put forward the effort of continuous monitoring, in order to be able to assess the ecological impact of LED lighting. Similarly, our study also implies that without assessing how a city replaces and maintains its public lighting assets, an observed decrease in sky brightness is not sufficient in predicting the ecological consequences of the public lighting scheme. Therefore, any future studies in long-term night sky monitoring must take into account the maintenance status of the public lighting assets to accurately reflect the ecological impacts.

6   Conclusion and outlook

THE BEGINNING of light pollution research, almost a century ago [52], concerned mostly the mortality of birds due to the presence of artificial light at night. Through various research the extensive negative effects of artificial light at night not only on ecology, but also on physiology, astronomy, energy consumption, and social impact in general. We need to measure the night sky because all these impacts depend on the pattern of artificial lightings. As light technologies are continuously developing, and human behavior, which can influence the use of artificial light, is difficult to predict, we must monitor the night sky to assess the changes in ecological and social impacts. In addition, night sky monitoring is an essential part for policy making in urban lighting plan, and potentially legislations regarding the use of outdoor lighting. The continuous development of aerospace and sensor technologies enable us to carry out remote sensing from the space and from the ground, providing us a tool for light pollution-related studies and policy making.

After the launch of the Suomi NPP satellite, the VIIRS–DNB sensor on board have been previously used to quantify upwelling artificial light as a means of studying light pollution in a global scale [20]. Efforts are also made to measure aerosol during night time using the upwelling artificial light [43]. While the angular distribution of artificial light can impact the skyglow pattern, even far away from the urban light dome [4], no systematic, wide area studies in the scale of continent have yet been done. Therefore, we used the data acquired in 2015 from VIIRS–DNB sensor to study the angular distribution of the emissions of artificial light. Although we encountered some problems for the measurements, such as the sensor being a broadband one not sensitive to blue light, difficulty in downloading the data, uncertainty of the measurements, the limited temporal coverage, and the low number of measurements due to the orbit of the satellite and sky condition, we are able to investigate the pattern of upwelling emission of light for major cities and metropolitan regions in Europe. We find that cities in Europe, with some exceptions, emit more light at high zenith angle (Figures 3.6 and 3.8). As upwelling light near the horizon can travel far away from the source, this implies that migratory animals which are active during the night time can easily be distracted by the light dome from a city far away in an otherwise natural area. To anticipate the increasing use of light sources with high color temperature, multispectral sensors which are sensitive enough for night time applications may be designed, built and launched in the future.

While satellite-based observations are useful in wide area surveys, ground-based, localized measurements have an advantage of more frequent data acquisitions, and usually have better signal quality. Low-cost sensors dedicated for night sky measurements, like the Sky Quality Meters (SQM) used in Chapters 4 and 5, enable ground-based short and long-term measurements for multiple locations. In 2011 and 2012, a worldwide study

of night sky, compiling and analyzing data of SQM measurements from 44 locations around the globe was conducted, and was the first time comparing ground-based night sky measurement data in a unified way. Analyzing the dataset as a whole, we found that the presence of artificial light reverses the variation pattern of the night sky when clouds are present, where weak, natural light sources are blocked by clouds from arriving at the ground level. Instead, clouds backscatter the emitted artificial light, brightening the night sky (Figure 4.5a and Table 4.3). The sky brightness is not constant when excluding major natural light sources, but in general darkens as the night progresses, when human activities decrease progressively through the night (Figure 4.6). Strong natural light sources, like the moon, no longer dominates the variation of the night sky brightness, but instead it depends on the cloud cover (Figure 4.8 and Table 4.6) [33]. In addition to these findings, we used the data of two sites from the campaign with both weather data, to compare with daytime aerosol measurements from the Aerosol Robotic Network (AERONET), and found that while it is not possible to establish a consistent relationship between the aerosol content in the atmosphere and sky brightness for the rural site in Cabauw, the Netherlands (Figure 4.10), the presence of aerosols brightens up the sky in Madrid (Figure 4.11).

Long-term monitoring enables us to find out the change in skyglow pattern over a long period. We therefore have been continuously measuring the night sky of Bremen, Germany using two SQMs, one in the suburban location of the campus of the University of Bremen, and the other one in the village Seebergen at the rural area just outside of the border of Bremen. The night sky of the suburban site at the university campus is found to be typical of a light-polluted location, with cloudy sky being brighter than clear sky and the skyglow becomes darker during the course of the night (Figures 5.6a and 5.7a. We found that while instrumental issues cannot be ruled out, over a span of about 4.5 years, the night sky brightness of the site has decreased, with midnight sky brightness decreasing annually by approximately 2.4% under clear sky, and 6.4% under overcast sky. In addition the decreasing trend was found to be stronger at the later hours of the night (Figures 5.8a and 5.9a). For the rural site it was found that in the early hours of the night, the local public and domestic lightings are the dominating light source for the skyglow, which also contributes to the larger brightening when the sky is cloudy. However, as the public and domestic lighting are progressively switched off, the night sky of the site exhibits characteristics typical with less light-polluted areas, where overcast sky is only slightly brighter or darker than clear sky (Figures 5.6b and 5.7b). As the progress replacing the public lighting to LED-based devices are slow, I suspect that the darkening of the night sky originates from the gradual decrease of output of the public lighting system due to aging, and that an improvement in terms of ecological impacts is not guaranteed. We can therefore expect that when the rate of light fixture replacement is accelerated in the future, we can see an increase of sky brightness. A survey on public lighting assets may also help predicting future trend of night sky brightness.

We also attempted to measure the blue content of Bremen's night sky using a ccd spectrometer. While we are not yet able to quantify this due to lack of instruments and other operational issues with the spectrometer, we found that even a zenith-pointing device can at least qualitatively observe the skyglow at some specific wavelengths. Shall the issues with the instruments be solved, this will potentially help us experimentally find out the long-term change in spectrum of the night sky with the introduction of led-based public lightings. Similarly, these ground-based long-term monitoring can be applied to locations worldwide, and together with satellite-based data, will provide valuable assets for not only environmental impact assessment, but also for policy makers to find out appropriate solutions of the problem of light pollution.

Bibliography

[1] Joint Polar Satellite System (JPSS) Visible Infrared Imaging Radiometer Suite (VIIRS) Sensor Data Records (SDR) Algorithm Theoretical Basis Document (ATBD). Algorithm theoretical basis document, National Oceanic and Atmospheric Administration, College Park, MD, USA, December 2013.

[2] Joint Polar Satellite System (JPSS) VIIRS Cloud Mask (VCM) Algorithm Theoretical Basis Document (ATBD). Algorithm theoretical basis document, National Aeronautics and Space Administration, Greenbelt, MD, USA, December 2014.

[3] J. Aceituno, S. F. Sánchez, F. J. Aceituno, D. Galadí-Enríquez, J. J. Negro, R. C. Soriguer, and G. S. Gomez. An All-Sky Transmission Monitor: ASTMON. *Publications of the Astronomical Society of the Pacific*, 123(907):1076–1086, 2011.

[4] M. Aubé. Physical behaviour of anthropogenic light propagation into the nocturnal environment. *Philosophical Transactions of the Royal Society of London B: Biological Sciences*, 370(1667), 2015.

[5] M. Aubé and M. Kocifaj. Using two light-pollution models to investigate artificial sky radiances at canary islands observatories. *Monthly Notices of the Royal Astronomical Society*, 422(1):819–830, 2012.

[6] M. Aubé, M. Kocifaj, J. Zamorano, H. S. Lamphar, and A. S. de Miguel. The spectral amplification effect of clouds to the night sky radiance in Madrid. *Journal of Quantitative Spectroscopy and Radiative Transfer*, 181:11–23, 2016. Special issue on *Using remote sensing to better understand light pollution (Light Pollution Theory Modelling and Measurements 2015)*.

[7] Y. Bai, C. Cao, and X. Shao. Assessment of scan-angle dependent radiometric bias of Suomi-NPP VIIRS day/night band from night light point source observations. In *Earth Observing Systems XX*, volume 9607 of *Proccedings of SPIE*, page 960727, 2015.

[8] K. Baugh, F.-C. Hsu, C. D. Elvidge, and M. Zhizhin. Nighttime Lights Compositing Using the VIIRS Day-Night Band: Preliminary Results. *Proceedings of the Asia-Pacific Advanced Network*, 35:70–86, 2013.

[9] R. L. Berry. Light Pollution in Southern Ontario. *Journal of the Royal Astronomical Society of Canada*, 70:97–115, June 1976.

[10] C. F. Bohren and D. R. Huffman. *Absorption and scattering of light by small particles*, pages 477–482. John Wiley & Sons, 1998.

[11] M. J. Brodzik, B. Billingsley, T. Haran, B. Raup, and M. H. Savoie. Ease-grid 2.0: Incremental but significant improvements for earth-gridded data sets. *ISPRS International Journal of Geo-Information*, 1(1):32, 2012.

[12] P. Cinzano. Night Sky Photometry with Sky Quality Meter. ISTIL Internal Report n. 9, v 1.4, ISTIL, Thiene, 2005.

[13] P. Cinzano. Report on Sky Quality Meter, version L. ISTIL Internal Report v 0.9, ISTIL, Thiene, 2007.

[14] P. Cinzano, F. Falchi, and C. D. Elvidge. The first world atlas of the artificial night sky brightness. *Monthly Notices of the Royal Astronomical*

Society, 328(3):689–707, 2001.

[15] Commission Internationale de l'Eclairage. Photometry - The CIE System of Physical Photometry. ISO 23539:2005(E) / CIE S 010/E:2004, 2005.

[16] D. M. Duriscoe. Measuring anthropogenic sky glow using a natural sky brightness model. *Publications of the Astronomical Society of the Pacific*, 125(933):1370–1382, 2013.

[17] D. M. Duriscoe. Photometric indicators of visual night sky quality derived from all-sky brightness maps. *Journal of Quantitative Spectroscopy and Radiative Transfer*, 181:33–45, 2016. Special issue on *Using remote sensing to better understand light pollution* (*Light Pollution Theory Modelling and Measurements 2015*).

[18] C. Elachi and J. van Zyl. *Introduction to the Physics and Techniques of Remote Sensing*, pages 72–73. John Wiley & Sons, Inc., Hoboken, NJ, USA, 2006.

[19] C. D. Elvidge and T. J. Walrave. AVIRIS observations of nocturnal lighting. In AVIRIS *Airborne Geosciences Workshop Proceedings, JPL*, pages ELV–1–3, 1999.

[20] F. Falchi, P. Cinzano, D. Duriscoe, C. C. M. Kyba, C. D. Elvidge, K. Baugh, B. A. Portnov, N. A. Rybnikova, and R. Furgoni. The new world atlas of artificial night sky brightness. *Science Advances*, 2(6), 2016.

[21] H. Farr. *Deutschlands höchste Gipfel: 35 Touren von der Küste bis zu den Alpen.*, pages 32–35. Books on Demand, Norderstedt, Germany, 2009.

[22] S. H., B. S. S., K. W. Wong, S. J., C. D. Elvidge, I. B. Pollack, T. B. Ryerson, W. P. Dube, N. L. Wagner, and D. D. Parrish. City lights and urban air. *Nature Geoscience*, 4(11):730–731, 11 2011. 10.1038/ngeo1300.

[23] A. Hänel. The increase in light pollution in central Europe as documented on DMSP data. In *Proceedings of the Dark-Skies Symposium*, Portsmouth, UK, 2006.

[24] B. Holben, T. Eck, I. Slutsker, D. Tanré, J. Buis, A. Setzer, E. Vermote, J. Reagan, Y. Kaufman, T. Nakajima, F. Lavenu, I. Jankowiak, and A. Smirnov. AERONET — A Federated Instrument Network and Data Archive for Aerosol Characterization. *Remote Sensing of Environment*, 66(1):1–16, 1998.

[25] C. S. Holt and T. F. Waters. Effect of Light Intensity on the Drift of Stream Invertebrates. *Ecology*, 48(2):225–234, 1967.

[26] S. R. James, R. W. Dennell, A. S. Gilbert, H. T. Lewis, J. A. J. Gowlett, T. F. Lynch, W. C. McGrew, C. R. Peters, G. G. Pope, A. B. Stahl, and S. R. James. Hominid Use of Fire in the Lower and Middle Pleistocene: A Review of the Evidence [and Comments and Replies]. *Current Anthropology*, 30(1):1–26, 1989.

[27] H. L. Johnson and W. W. Morgan. Fundamental stellar photometry for standards of spectral type on the revised system of the Yerkes spectral atlas. *Astrophysical Journal*, 117:313–352, May 1953.

[28] D. W. Johnston and T. P. Haines. Analysis of Mass Bird Mortality in October, 1954. *The Auk*, 74(4):447–458, 1957.

[29] M. Kocifaj and H. A. Solano Lamphar. Quantitative analysis of night skyglow amplification under cloudy conditions. *Monthly Notices of the Royal Astronomical Society*, 443(4):3665–3674, 2014.

[30] H. Kuechly, C. Kyba, T. Ruhtz, C. Lindemann, C. Wolter, J. Fischer, and F. Hölker. Aerial survey and spatial analysis of sources of light pollution

in Berlin, Germany. *Remote Sensing of Environment*, 126:39–50, 2012.

[31] C. Kyba, T. Ruhtz, C. Lindemann, J. Fischer, and F. Hölker. Two camera system for measurement of urban uplight angular distribution. *AIP Conference Proceedings*, 1531(1):568–571, 2013.

[32] C. C. M. Kyba, T. Ruhtz, J. Fischer, and F. Hölker. Red is the new black: how the colour of urban skyglow varies with cloud cover. *Monthly Notices of the Royal Astronomical Society*, pages 701–708, 2012.

[33] C. C. M. Kyba, K. P. Tong, J. Bennie, I. Birriel, J. J. Birriel, A. Cool, A. Danielsen, T. W. Davies, P. N. den Outer, W. Edwards, R. Ehlert, F. Falchi, J. Fischer, A. Giacomelli, F. Giubbilini, M. Haaima, C. Hesse, G. Heygster, F. Hölker, R. Inger, L. J. Jensen, H. Kuechly, J. Kuehn, P. Langill, D. Lolkema, M. Nagy, M. Nievas, N. Ochi, E. Popow, T. Posch, J. Puschnig, T. Ruhtz, W. Schmidt, R. Schwarz, A. Schwope, H. Spoelstra, A. Tekatch, M. Trueblood, C. E. Walker, M. Weber, D. L. Welch, J. Zamorano, and K. J. Gaston. Worldwide variations in artificial skyglow. *Scientific reports*, 5, 2015.

[34] C. C. M. Kyba, J. M. Wagner, H. U. Kuechly, C. E. Walker, C. D. Elvidge, F. Falchi, T. Ruhtz, J. Fischer, and F. Hölker. Citizen science provides valuable data for monitoring global night sky luminance. *Scientific Reports*, (1835), 2013.

[35] H. A. S. Lamphar and M. Kocifaj. Urban artificial light emission function determined experimentally using night sky images. *Journal of Quantitative Spectroscopy and Radiative Transfer*, 181:87–95, 2016. Special issue on *Using remote sensing to better understand light pollution* (*Light Pollution Theory Modelling and Measurements 2015*).

[36] C. Leinert, S. Bowyer, L. Haikala, M. Hanner, M. Hauser, A.-C. Levasseur-Regourd, I. Mann, K. Mattila, W. Reach, W. Schlosser, H. Staude, G. Toller, J. Weiland, J. Weinberg, and A. Witt. The 1997 reference of diffuse night sky brightness. *Astronomy and Astrophysics Supplement Series*, 127(1):1–99, 1998.

[37] H. Letu, G. Tana, M. Hara, and F. Nishio. Monitoring the electric power consumption by lighting from DMSP/OLS nighttime satellite imagery. In *2011 IEEE International Geoscience and Remote Sensing Symposium (IGARSS)*, pages 2113–2116, July 2011.

[38] Q. Li, T. Zheng, T. R. Holford, P. Boyle, Y. Zhang, and M. Dai. Light at night and breast cancer risk: results from a population-based case-control study in Connecticut, USA. *Cancer Causes & Control*, 21(12):2281–2285, 2010.

[39] K. N. Liou. *An introduction to atmospheric radiation*, volume v 84 of *International geophysics series*, pages 87–93. Academic Press, Amsterdam, 2002.

[40] Z. Liu, C. He, and Y. Yang. Mapping urban areas by performing systematic correction for DMSP/OLS Nighttime Lights Time Series in China from 1992 to 2008. In *2011 IEEE International Geoscience and Remote Sensing Symposium (IGARSS)*, pages 1858–1861, July 2011.

[41] T. Longcore and C. Rich. Ecological Light Pollution. *Frontiers in Ecology and the Environment*, 2(4):191–198, 2004.

[42] C. B. Luginbuhl, P. A. Boley, and D. R. Davis. The impact of light source spectral power distribution on sky glow. *Journal of Quantitative*

Spectroscopy and Radiative Transfer, 139:21–26, 2014. Special issue on *Light pollution: Theory, modeling, and measurements*.

[43] T. M. McHardy, J. Zhang, J. S. Reid, S. D. Miller, E. J. Hyer, and R. E. Kuehn. An improved method for retrieving nighttime aerosol optical thickness from the VIIRS Day/Night Band. *Atmospheric Measurement Techniques*, 8:4773–4783, Nov. 2015.

[44] G. Mie. Beiträge zur Optik trüber Medien, speziell kolloidaler Metallösungen. *Annalen der Physik*, 330(3):377–445, 1908.

[45] S. D. Miller, S. P. Mills, C. D. Elvidge, D. T. Lindsey, T. F. Lee, and J. D. Hawkins. Suomi satellite brings to light a unique frontier of nighttime environmental sensing capabilities. *Proceedings of the National Academy of Sciences*, 109(39):15706–15711, 2012.

[46] National Institute of Standard and Technology (NIST). *Persistent Lines of Neutral Mercury* (HgI). Accessed December 2016. http://physics.nist.gov/PhysRefData/Handbook/Tables/mercurytable3.htm.

[47] K. J. Navara and R. J. Nelson. The dark side of light at night: physiological, epidemiological, and ecological consequences. *Journal of Pineal Research*, 43(3):215–224, 2007.

[48] E. Peters, F. Wittrock, K. Großmann, U. Frieß, A. Richter, and J. P. Burrows. Formaldehyde and nitrogen dioxide over the remote western Pacific Ocean: SCIAMACHY and GOME−2 validation using ship-based MAX-DOAS observations. *Atmospheric Chemistry and Physics*, 12(22):11179–11197, 2012.

[49] M. Pravettoni, D. Strepparava, N. Cereghetti, S. Klett, M. Andretta, and M. Steiger. Indoor calibration of sky quality meters: Linearity, spectral responsivity and uncertainty analysis. *Journal of Quantitative Spectroscopy and Radiative Transfer*, 181:74 – 86, 2016. Special issue on *Using remote sensing to better understand light pollution* (*Light Pollution Theory Modelling and Measurements 2015*).

[50] K. W. Riegel. Light Pollution. *Science*, 179(4080):1285–1291, 1973.

[51] K. A. Robert, J. A. Lesku, J. Partecke, and B. Chambers. Artificial light at night desynchronizes strictly seasonal reproduction in a wild mammal. *Proceedings of the Royal Society of London B: Biological Sciences*, 282(1816), 2015.

[52] W. Rowan. Relation of Light to Bird Migration and Developmental Changes. *Nature*, 115:494–495, 1925.

[53] M. Royer. Lumen Maintenance and Light Loss Factors: Consequences of Current Design Practices for LEDs. *LEUKOS*, 10(2):77–86, 2014.

[54] R. Salgado-Delgado, A. T. Osorio, N. Saderi, and C. Escobar. Disruption of Circadian Rhythms: A Crucial Factor in the Etiology of Depression. *Depression Research and Treatment*, 2011, 2011.

[55] C. W. So. Observational studies of the night sky in Hong Kong. Master of philosophy thesis, The University of Hong Kong, Hong Kong, 2010.

[56] C. W. So. *Observational studies of contributions of artificial and natural light factors to the night sky brightness measured through a monitoring network in Hong Kong* . PhD thesis, The University of Hong Kong, 2014.

[57] C. W. So and J. C. S. Pun. Report of A Survey of Light Pollution in Hong Kong. Project report, The University of Hong Kong, Hong Kong,

2010.

[58] H. Stark, S. S. Brown, W. P. Dube, N. Wagner, T. B. Ryerson, I. B. Pollack, and D. D. Parrish. Nighttime photochemistry: nitrate radical destruction by anthropogenic light sources. *AGU Fall Meeting Abstracts*, page C117, 12 2010.

[59] R. G. Stevens. Light-at-night, circadian disruption and breast cancer: assessment of existing evidence. *International Journal of Epidemiology*, 38(4):963–970, 2009.

[60] A. Sánchez de Miguel. *Variación espacial, temporal y espectral de la contaminación lumínica y sus fuentes: Metodología y resultados*. PhD thesis, Universidad Complutense de Madrid, 2015.

[61] A. Tekatch. SQM lens comparisons: Half-ball vs cone, IR filters, lens holders. Technical report, Unihedron, Grimsby, ON, Canada, 2016.

[62] K. P. Tong. Measurement of Zenith Night Sky Luminance in the City of Bremen and Surroundings. Master thesis, University of Bremen, Bremen, 2012.

[63] H. van de Hulst. *Light Scattering by Small Particles*. Dover Books on Physics. Dover Publications, New York, NY, USA, 1981.

[64] C. Vollmer, U. Michel, and C. Randler. Outdoor Light at Night (LAN) Is Correlated With Eveningness in Adolescents. *Chronobiology International*, 29(4):502–508, 2012.

[65] A. Weigert, H. J. Wendker, and L. Wisotzki. *Astronomie und Astrophysik : Ein Grundkurs*, page 43. Wiley-VCH, Weinheim, Germany, 2009.

[66] K. E. West, M. R. Jablonski, B. Warfield, K. S. Cecil, M. James, M. A. Ayers, J. Maida, C. Bowen, D. H. Sliney, M. D. Rollag, et al. Blue light from light-emitting diodes elicits a dose-dependent suppression of melatonin in humans. *Journal of Applied Physiology*, 110(3):619–626, 2011.

[67] D. R. Williams. *Earth Fact Sheet*. National Aeronautics and Space Administration (NASA) Goddard Space Flight Center, accessed December 2016. http://nssdc.gsfc.nasa.gov/planetary/factsheet/earthfact.html.

[68] World Metreological Organization. FM system of numbering code forms. *Manual of Codes, WMO No. 306*, I.1:A.1–A.71, 2009.

[69] X. Xiong, J. Butler, K. Chiang, B. Efremova, J. Fulbright, N. Lei, J. McIntire, H. Oudrari, Z. Wang, and A. Wu. Assessment of S-NPP VIIRS on-orbit radiometric calibration and performance. *Remote Sensing*, 8(2):84, 2016.

Epilogue

SIMILAR to most subjects in environmental sciences, light pollution research is necessary only because such a problem exists. And, like many other environmental issues, the problem of light pollution can at least be partially solved simply by self-regulating the use of lighting by individual users. While this thesis is far from being revolutionary, I hope that it can raise the awareness of individuals and society, to take a serious look into the problem, and turn this thesis into a mere record of our history.

Acknowledgements